http://eprints.gla.ac.uk/181659/

Deposited on: 13 March 2019

The turbulence modelling of a pulsed impinging jet using LES and a divergence free mass flux corrected turbulent inlet

Matthew Haines[a], Ian Taylor[a,b,1,*]

[a]*Department of Mechanical and Aerospace Engineering, University of Strathclyde, Glasgow, UK, G1 1XJ*
[b]*School of Engineering, James Watt Building South, University of Glasgow, Glasgow, G12 8QQ*

Abstract

This paper examines the best turbulence model to use when using computational fluid dynamics to simulate an impinging jet type flow. The IDDES, k-ω SST SAS, Smagorinsky and dynamic Smagorinsky models were used and compared to data collected from a laboratory impinging jet, developed to simulate thunderstorm downburst flow fields. From this it was found the dynamic Smagorinsky model performed best, especially at capturing the velocities and pressures in the near inlet region. A mesh dependency study was then performed for the dynamic Smagorinsky turbulence model. A small mesh dependency was demonstrated for the mesh densities studied but had issues in capturing the velocity height profile correctly in the near wall region. Despite this issue the model still closely matched the laboratory pressures around a $60\,mm$ cube and demonstrated the suitability of this modelling approach for investigating thunderstorm downbursts.

Keywords: Turbulence modelling, impinging jets, LES, downbursts, non-stationary analysis.

2010 MSC: 00-01, 99-00

*Corresponding author
*Email address:* `Ian.Taylor@glasgow.ac.uk` (Ian Taylor)
[1]Based at University of Strathclyde prior to 20 July 2016 and at University of Glasgow from 20 July 2016.

1. Introduction

A thunderstorm downburst is a strong wind event characterised by winds formed from a horizontally aligned vortex, itself formed from a strong downward movement of air arising from falling precipitation, buoyancy effects and intensified by other cloud processes such as the melting of ice and hail (Palmén, 1951; Roberts and Wilson, 1984; Fujita, 1985; Knupp, 1985). They are important from a wind engineering perspective as they are strongly non-stationary (Figure 1(a)) and also produce a different vertical velocity profile to the traditional logarithmic atmospheric boundary layer (ABL) profile used by wind engineers (Figure 1(b)).

In order to investigate their effects wind engineers make use of a number of modelling techniques, including both laboratory and numerical simulations. In the laboratory the most common approach is to use an impinging jet simulator (Holmes, 1992), where a jet of air is directed onto a plane perpendicular to the jet. This generates a vortex similar to that of a downburst, although the formation mechanisms are physically different.

There have also been numerically simulated impinging jet studies relating to downburst flow. The first was by Selvam and Holmes (1992), using the RANS $k - \epsilon$ turbulence model. Later work by Craft et al. (1993) found this model unsuitable because the turbulent kinetic energy was significantly over estimated. It was found that the rms turbulent velocity normal to the wall was over predicted by up to four times experimental values, which resulted in low level velocities being under predicted, high level velocities over predicted and as a result the vertical velocity profile was not reproduced correctly. As highlighted by Craft et al. (1993), this is primarily due to the use of the eddy-viscosity stress-strain law for normal stresses leading to high turbulence energy generation close the stagnation region. More recently Mason et al. (2007) evaluated six additional turbulence models using the impinging jet simulator of Mason et al. (2005) to validate results. Mason et al. (2007) found that of the five turbulence models it was the $k - \omega$ SST model which most accurately reproduced the flow from an

2
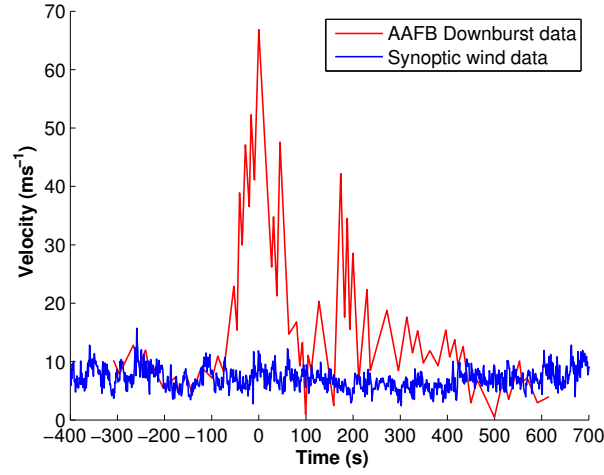
(a) Downburst velocity time history
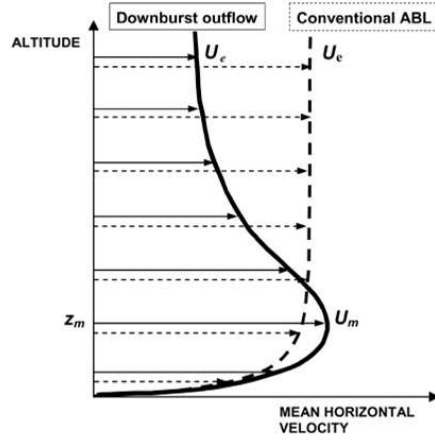
(b) Vertical velocity profile

Figure 1: Comparison of typical wind profiles for downburst and conventional ABL flows : (a) - a velocity time history comparison of a rural synoptic wind at $3\,m$ height (Sterling et al., 2006) and the Andrew's air force base (AAFB) downburst over rural terrain, $4.9\,m$ height, Fujita (1985); (b) - a schematic illustration of the mean streamwise velocity profile corresponding to a "typical" downburst and a typical boundary layer or "synoptic" wind (Lin and Savory, 2006).

impinging jet simulator. The only discrepancy being a slight over prediction of velocity at higher levels.

Further work in this field was carried out by Sengupta and Sarkar (2008) who used an LES based turbulence model, dynamic Smagorinsky-Lilly, to simulate a translating impinging jet. The results were again validated using data collected from a simulator also developed by Sengupta and Sarkar (2008). However, there is a potential difficulty with LES based simulations and impinging jets. For the boundary conditions to be stable a large domain is often required of around ten jet diameters meaning a large number of cells is required for the Y^+ value to be close to one with Y^+ defined as the non-dimensional wall distance:

$$Y^+ = \frac{u_* y}{\nu} \tag{1}$$

where u_* is traditionally the wall shear stress velocity or "friction velocity" of the near wall flow, y is the distance to the nearest wall and ν is the kinematic viscosity of the fluid.

The Y^+ value used by Sengupta and Sarkar (2008) in their simulations was not presented in their paper. However, they indicate that around 2 million cells were used to simulate a domain extending to a width of ≈ 15 jet diameters. Based on this information, it is estimated that it is unlikely that Y^+ values approaching unity were used in their simulations, though this cannot be stated with certainty with the information available. Assuming a relatively low peak velocity of $10 \, ms^{-1}$ such as the values recorded by Chay and Letchford (2002) the cell size in the near wall would have to be $3 \times 10^{-5} \, m$ to achieve $Y^+ = 1$.

However, the results presented in both Sengupta and Sarkar (2008) and Chay and Letchford (2002) matched well to experimental data, suggesting that satisfying the Y^+ criteria may not be essential for the simulation of impinging jets and this has implications for the work presented herein. A possible reason for the good performance of the LES models, despite the lack of wall resolution, is that the most important flow feature in a downburst / pulsed impinging jet flow is the primary vortex which is generated from shear layers in the free stream

flow. The strong effect of the primary vortex on the flow, as illustrated in Figure 1, combined with the predicted results from Sengupta and Sarkar (2008) and Chay and Letchford (2002) and those presented herein indicate turbulence which is generated at the wall is not the primary turbulence formation mechanism as is the case in channel flow.

The implication from this is the importance of producing the correct turbulence at the inlet, in this case, to match the laboratory simulation and the highly turbulent inlet of Jesson et al. (2015), (Figure 2). When comparing with this experimental dataset, there is a complication with achieving an exact comparison due to the nature of the "flaps" mechanism for the jet used in the experiment. This is highlighted in more detail in the next section and the approach taken in these simulations was to use the data measured $0.5\,m$ from the jet inlet as the basis for obtaining the correct inlet turbulence characteristics. CFD simulations often assume a laminar inlet or turbulent inlets based on Reynolds averaging of the Navier-Stokes equations (RANS), which will alter the development of the shear layer and therefore the rest of the flow. For RANS approaches, inflow boundary conditions may be based on averaged quantities, turbulence intensities and length scales, whereas for LES, much more detailed information is required to provide temporally varying information for velocities and pressures, often not directly available. Numerous approaches have been used to generate the turbulent inflow conditions to give realistic wind flow characteristics for ABL flows, for example Blocken et al. (2007), Parente et al. (2011), Zheng et al. (2012) and Balogh et al. (2012). Similarly, LES approaches using a synthetic turbulence approach to generate the inflow turbulence for ABL's have been applied to computational wind engineering investigations in Bazdidi-Tehrani et al. (2016), Patruno and Ricci (2017), Lamberti et al. (2018) and Yan and Li (2015). In particular Patruno and Ricci (2017) illustrates an approach that provides good control and accuracy of turbulent integral length scales and time spectra, with encouraging results for the turbulence intensities and length scales typical of ABL flows. Lamberti et al. (2018) illustrate how an automated approach is used to modify the input parameters for the turbulence

generator to maintain the desired turbulence statistics at a downstream location, in combination with a divergence free approach from Kim et al. (2013). However, a different approach is necessary for non-synoptic flow fields, as indicated by Kareem (2012). One approach is to generate the necessary information is to use approaches based on a synthetic turbulent inlet in order to accurately model the turbulence found at the inlet (di Mare et al., 2006). Furthermore, an appropriate turbulence model then needs to be identified that can successfully support fluctuations at the inlet that are being determined from the synthetic turbulent inlet and additionally allow them to propagate correctly throughout the domain (Kim et al. (2013) and Poletto et al. (2013)). Also important in this regard is the mesh density, a suitable mesh must be found which is the best balance between being accurate but not requiring excessive CPU time.

Usually an investigation of the mesh sensitivity would be the initial consideration for a CFD analysis. However, for this research, it was felt more appropriate to consider initially the implementation of the synthetic turbulent inlet and the implication of this boundary condition on the choice of turbulence model. Once the turbulence model was selected, a mesh sensitivity investigation was undertaken prior to analysis of the simulation results when compared to laboratory data. Hence, the work presented herein first provides a brief summary of the implementation of a synthetic turbulent inlet considering the difficulties and challenges encountered for an impinging jet simulation. Then a detailed investigation of a range of turbulence models is considered, highlighting their performance alongside the synthetic turbulent inlet. Finally a mesh sensitivity analysis is undertaken along with comparison of the results with experimental data. The outcome of the paper is the determination of appropriate modelling schemes for the boundary conditions and turbulence model, along with assessment of the mesh density (with particular consideration to the Y^+ criteria highlighted above) to provide high quality simulations of downburst / impinging jet flow fields. Further detailed analysis of the predicted flow field and comparison with laboratory data is presented in Haines and Taylor (2018), where the modelling approach determined from the results presented herein is

used to provide detailed assessment of the downburst flow. Additionally, investigation of the effects of the downburst on "low rise" buildings are discussed in Haines and Taylor (2018) where the simulations are used to assess and interpret some flow features arising in the pressure and drag coefficient results presented in the experiments of Jesson et al. (2015). Also a brief comparison of the flow features arising from the downburst flows, both simulated and experimental, with those from atmospheric boundary layer flows are discussed in Haines and Taylor (2018).
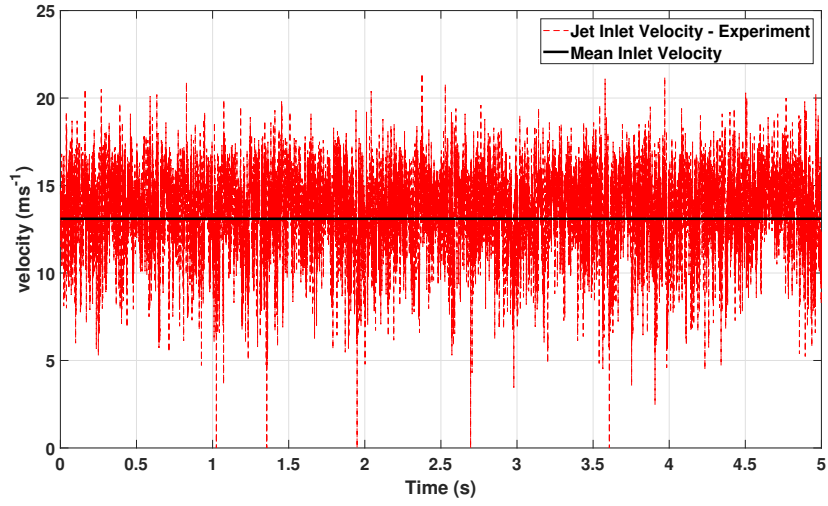

Figure 2: The velocity time history of the laboratory jet (Jesson et al., 2015) $0.5\,m$ from the jet inlet. The locations where the signal drop to zero represent probe drop outs and are not part of the turbulent component of the signal.

2. Numerical Setup

The coordinate system used in the simulations is illustrated in Figure 3, and is based on the University of Birmingham simulator (Jesson et al. (2015). X is the distance from the centre of the jet, running down the centreline of the simulator, Y the spanwise position across the width of the simulator and Z the

height from the floor of the simulator. These were normalised by the width of the jet of the simulator D, which in the laboratory was $1\,m$.

The numerical domain was created to ensure the measurement locations used in Jesson et al. (2015) were covered and to allow data collection with sufficient resolution and over a reasonable time-scale The key measurement locations from the experiment were $0.5\,m$ below the jet inlet (in the centre of the jet) and then at various locations along the centreline, $\frac{X}{D} = 1.0$, 1.5, 2.0 and 2.5. At each $\frac{X}{D}$ distance twenty five heights were measured between $\frac{Z}{D} = 0.01 - 0.25$. At these points the three components of velocity were captured as well as the pressure field. Additionally a cube model building was placed into the flow in the laboratory case, located at $\frac{X}{D} = 1.5$, $\frac{Y}{D} = 0.0$. Full details of the measurement techniques used in the laboratory experiments are provided in Jesson et al. (2015).

The open source software, OpenFOAM [2] ((OpenFOAM, 2014)) was used to create the domain and perform the CFD calculations, with custom solvers and boundary conditions being implemented where necessary. The numerical domain used is illustrated in Figure 4(a) and is a $10 \times 10 \times 2.5\,m$ box (Figure 3(b)), with a cylindrical inlet with a mesh consisting of $15,338,950$ hexahedral elements with every cell having an aspect ratio of 1. The building can be seen on the right hand side of Figure 4(a) with the local mesh around the building illustrated in Figure 4(b). In the near building region the mesh had a cell size of $1.25\,mm$ and near the inlet and in the free stream a cell size of $20\,mm$. The cell size of $1.25\,mm$ was used up to a distance $30\,mm$ from the building, then a cell size of $2.5\,mm$ from $30\,mm - 60\,mm$, cell size $5\,mm$ from $60\,mm - 120\,mm$, cell size $10\,mm$ from $120\,mm - 180\,mm$, and cell size $20\,mm$ at distances greater than $180\,mm$. $4:1$ face transitions are used throughout the mesh, and although such transitions lead to numerical and commutation errors, the small and continuous change in cell sizes highlighted keep these errors to a minimum. Results presented in Haines and Taylor (2018) show that

---

[2]Ver. 2.2.2 of OpenFOAM was used for these simulations, undertaken during 2015/16

8
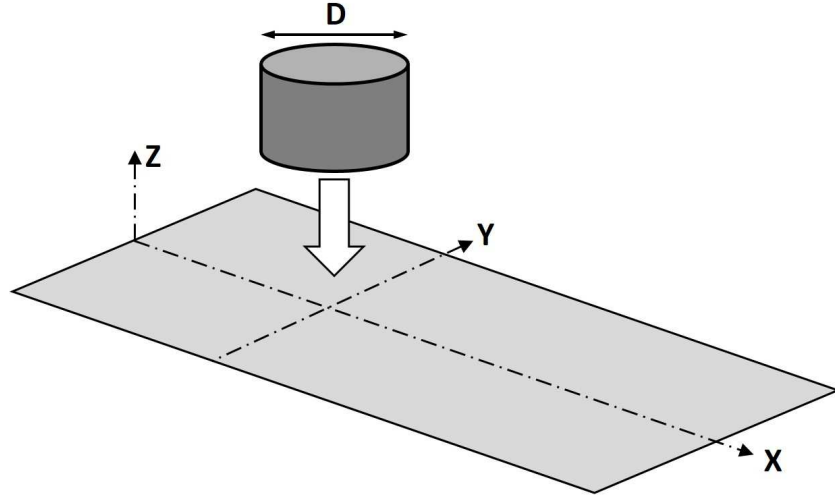
(a) Schematic diagram of the numerical domain for the simulations
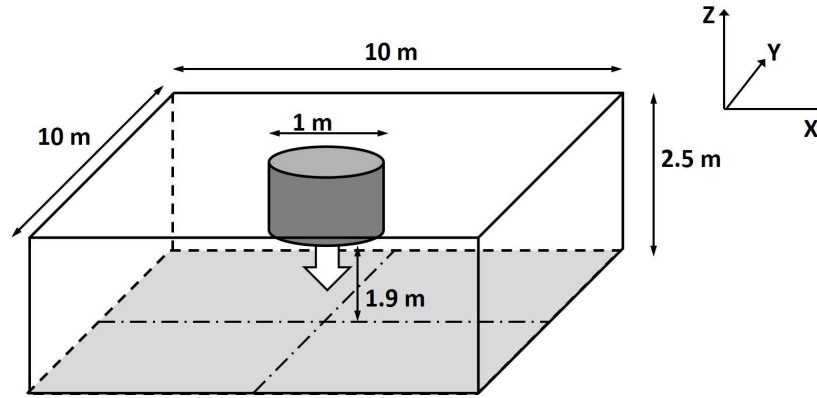
(b) Dimensions of numerical domain for the simulations - jet inlet is $1.9\,m$ above the ground plane.

Figure 3: Schematic diagram of the numerical domain for the simulations, based on the University of Birmingham simulator. The labels X, Y and Z highlight the direction of the coordinate system.

the transitions have little effect on the overall results.

The cell size at the jet inlet measurement location ($0.5\,m$ below the inlet) is the same as the free stream cell size, also $20\,mm$. At peak velocity ($21\,ms^{-1}$) due to the primary vortex, it was found that the Y^+ in the near building region was $\approx$ 100, far greater than the usual required value for wall resolved LES simulations for turbulent fluctuations within the boundary layer. However, assessment of the effect of this will be examined later. Two additional mesh densities were also trialled to verify the solution demonstrated little or negligible mesh dependency, a coarser $11,054,940$ cell mesh and a finer $20,154,014$ cell mesh. In these two cases in the free stream region a cell size of $23\,mm$ and $17\,mm$ was found respectively and in the near building region $1.4\,mm$ and $1.1\,mm$ and the results of mesh sensitivity will be discussed after the assessment of the turbulence modelling scheme.
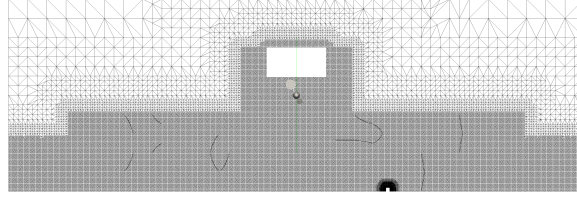
(a) Numerical model domain and mesh
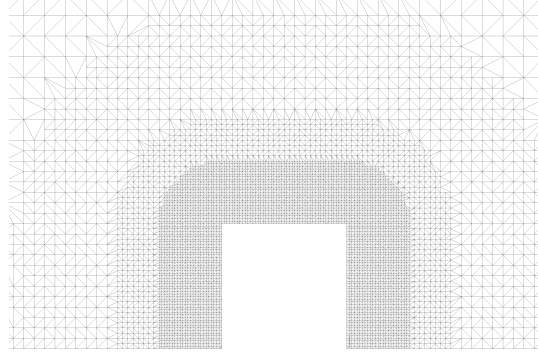
(b) Mesh detail around the cube building

Figure 4: Numerical model domain and mesh with detail around the cube building

The boundary conditions at the inlet were a jet of uniform profile, with a

component of velocity in the z (downwards) direction of $13.4\,ms^{-1}$ (Jesson et al., 2015), with synthetic turbulence added, as detailed further below and zero gradient boundary condition for pressure. The OpenFOAM library PisoFoam [3] is used as the basis for the flow solver in each case, with time step set to $5 \times 10^{-7}\,s$, but with adjustable time step selected [4] using a maximum ΔT of $0.1\,s$ and maximum Courant number of 0.5. The time derivative approximation "backward" was used to avoid dissipation. The spatial approximations were set to the following: gradSchemes "Gauss Linear"; divSchemes "Gauss Linear"; laplacianSchemes "Gauss Linear Corrected" due to the non-orthogonal cells around the cylindrical inlet; interpolationSchemes "linear"; snGradSchemes "corrected" as it gives an explicit non-orthogonal correction to the surface normal gradient calculation, necessary due to cells around the cylindrical inlet.

It should be noted that the jet generation mechanism between the CFD and laboratory simulation differed. The laboratory simulation used a "flaps" mechanism, which is described in Jesson et al. (2015), whereas the CFD simulation just used an open jet. The "flaps" mechanism probably introduced some differences to the inlet flow, firstly the jet was not an instantaneous $1\,m$ wide as it was in the CFD, instead a narrow jet was formed initially as the flaps swung open which then rapidly increased in width until $1\,m$ wide. Secondly the air flow from the flaps may have interfered with the vortex formation, potentially reducing its size or causing it to decay more rapidly than in the CFD simulation. However, the exact effect of the flaps in the laboratory simulator is not known and was not measured. Whilst the flaps mechanism could be simulated, the computational cost would be high and with the available information, it is unclear how much effect this will have on the accuracy of the simulation.

For downburst type flows, surface roughness is felt to affect the formation of the secondary vortex (Mason et al., 2009), though does not affect the shape or

---

[3] Solvers used "GAMG" for pressure and "DILUPBiCG" for velocity.

[4] The iterative convergence criteria used "myCFLPISO" with the adjustable timestep depending on Courant number. In all cases, the residuals were of the order 10^{-4} or lower.

development of the main flow feature, the primary vortex (Vermeire et al., 2011). For the experimental facility, the distance between the point of impingement of the jet and the location of the peak wind speed is relatively small, "indicating that surface roughness is not a governing factor" in the laboratory simulator (Jesson et al., 2015). Based on this assumption and to reduce complexity of the CFD models, surface roughness was not modelled or included in the simulations.

The sides of the domain and also the top (above the jet inlet), were treated as outlets and a Neumann (zero gradient) boundary was used. These boundary conditions are applied also to determine any inflow/outflow at the sides of the domain, though typically the simulations are ended before the primary vortex reaches the edge of the domain and hence before the effects of flow across the boundaries become significant. The wall boundary conditions used no slip for velocity and zero gradient for pressure. For post-processing of results, pressures are presented as pressure coefficients rather than dimensioned properties, where (2) is used to determine the pressure coefficient, C_p,

$$C_p = \frac{p - p_{ref}}{\frac{1}{2}\rho U^2} \tag{2}$$

where p is the pressure value from experiment or simulation, p_{ref} is a reference pressure, in this case atmospheric pressure consistent with the approach used in the experiments (Jesson et al., 2015) and U is the reference velocity. For the results at the jet inlet, the reference velocity used in (2) is the inlet velocity $U = 13.4\,ms^{-1}$. However, for the impinging flow on the ground surface and building surfaces, the peak velocity of the downburst flow of $U = 21.0\,ms^{-1}$ is used, consistent with Jesson et al. (2015) and Haines and Taylor (2018). At the jet inlet, using the inlet velocity of $13.4\,ms^{-1}$ for the reference velocity when calculating C_p is an obvious choice. However due to the transient nature of the flow at the building location, and the effect of the primary vortex on the flow (e.g. Figure 1b) using the jet velocity in this location is not as appropriate. Using the peak velocity of the primary vortex was used a more relevant selection for the reference velocity to determine C_p at the building location and to allow comparison with previously published work, has also been used herein.

## 2.1. Synthetic turbulence at the impinging jet inlet

In order to accurately simulate the impinging jet simulator at the University of Birmingham the turbulence at the inlet of the simulator must be correctly modelled to ensure the correct development of the flow further downstream and as discussed briefly above (di Mare et al., 2006), for LES a synthetic turbulent inlet is required. There are a number of approaches to generate synthetic turbulence including: superimposing random fluctuations; Fourier series based approaches which generate frequencies of turbulence based on the power spectral density (PSD) of a known experimental time series (Billson et al., 2003); reconstructing an experimental data time series, for example the wavelet methods developed by Wang et al. (2013), then interpolating this field across a CFD inlet; methods based upon digital filters and finding solutions for specific autocorrelation functions (Kornev and Hassel, 2007); vorticity based approaches which use Lagrangian based vortex methods to generate turbulence using a "vortex in a box" approach (Poletto et al., 2013).

Initially the turbulence model of Billson et al. (2003), based on Fourier and frequency techniques was chosen as the approach was similar to wind tunnel analysis, by matching the PSD and turbulent length scales from full scale data (Haines et al. (2015)). However, whilst capable of producing a velocity field which closely matched the inlet data from the laboratory simulations (Figure 5(a)) it could not reproduce the pressure field, illustrated in Figure 5(b). The reason for this discrepancy can be found in the incompressible Navier-Stokes equations, the PISO algorithm and in the formulation of the synthetic turbulent inlet of Billson et al. (2003).
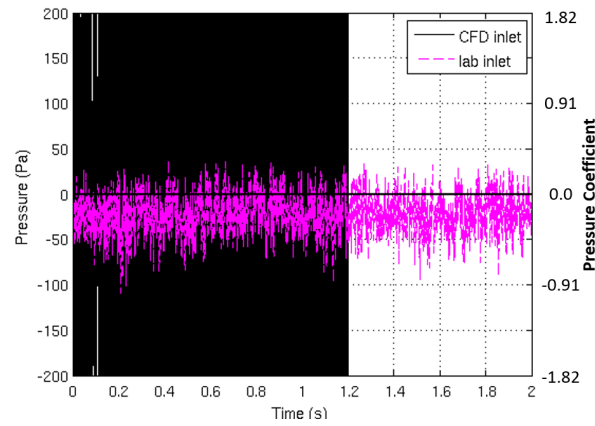
Firstly the Navier-Stokes equations in incompressible form assume that the net mass flux through each cell is zero, as shown by equation (3) (in incompressible form) :

$$\nabla \cdot \mathbf{V} = 0 \tag{3}$$

where $\mathbf{V}$ is the velocity vector of the flow.
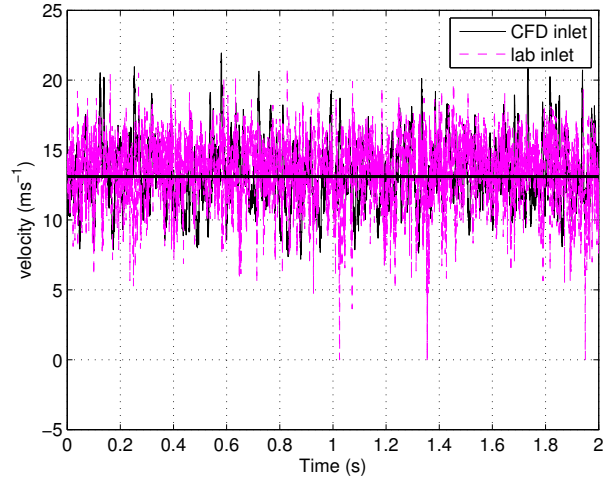
(a) Velocity fluctuations

(b) Pressure fluctuations

Figure 5: Results of CFD simulation of jet inlet flow compared to the laboratory experiment at a distance $0.5\,m$ from the jet inlet. (a) - the turbulent velocity fluctuations produced $0.5\,m$ from the inlet, CFD and experiment; (b) - the associated unphysical pressure fluctuations from the CFD simulation compared to the pressure fluctuations from the laboratory simulator.

14

Unfortunately this is not true of the turbulent inlet of Billson et al. (2003), and the turbulence it produces is not divergence free, i.e. equation (3) is not obeyed across the inlet. Hence the PISO algorithm itself has to make the flow divergence free, which, in order to support such velocity fluctuations, requires a rapidly fluctuating pressure field, hence giving the result in Figure 5(b).

An alternative divergence free approach based on the digital filter method (often called the random spot method) developed by Kornev and Hassel (2007) which was chosen as it was available pre-coded in OpenFOAM as part of the add on LEMOS package (LEMOS, 2015). This method uses the Reynolds stress tensor (equation (4)) and integral length scale (equation (5)) to produce synthetic turbulence with a two point spatial correlation, one point temporal correlation and a one point cross correlation. The Reynolds stress tensor, τ_{ij} is given by

$$\tau_{ij} = \begin{Bmatrix} \rho \, \overline{u'u'} & \rho \, \overline{u'v'} & \rho \, \overline{u'w'} \\ \rho \, \overline{v'u'} & \rho \, \overline{v'v'} & \rho \, \overline{v'w'} \\ \rho \, \overline{w'u'} & \rho \, \overline{w'v'} & \rho \, \overline{w'w'} \end{Bmatrix} \tag{4}$$

where u', v', w' represent the fluctuating components of velocity in the u, v and w directions respectively. Also, the integral length scale, L_{iik}, is given at an inlet plane by

$$L_{ii1}\left(x\right) = \int_{-\infty}^{\infty} R_{ii}\left(\mathbf{x}, \mathbf{x} + \mathbf{i}\eta\right) d\eta, \tag{5a}$$

$$\text{where } R_{ii}\left(\mathbf{x}, \mathbf{x} + \eta\right) = \frac{\overline{u_i\left(\mathbf{x}, t\right) u_i\left(\mathbf{x} + \eta, t\right)}}{\overline{u_i\left(\mathbf{x}, t\right)}^2} \tag{5b}$$

where $R_{ii}\left(\mathbf{x}, \mathbf{x} + \eta\right)$ is the autocorrelation of the signal, t is a timestep in the signal and η is the shift in signal to the point in the signal for which the autocorrelation is being calculated for position x (Kornev and Hassel, 2007).

Figure 6(a), illustrates that even this divergence free condition did not produce a satisfactory pressure field. It was noted that the finite size of the inlet meant that the instantaneous mass flux entering the computational domain was not equal to the mass flux expected from the mean field, which again resulted in

the PISO algorithm producing unrealistic pressure fluctuations. To resolve this a mass flux correction term from Kim et al. (2013) and Poletto et al. (2013), given by equation (6) was applied to the flow field across the inlet, this reduced the pressure fluctuations to slightly above the laboratory case, as illustrated in Figure 6(b).

$$u_i = \frac{U_b}{U_{b,T}} u_{i,T}, \quad \text{where} \quad U_{b,T} = \frac{\int_S U_{n,T} dS}{S} \tag{6}$$

where u_i is the final instantaneous mass flux corrected turbulent velocity field produced at the inlet, U_b is the bulk flow field prior to turbulent fluctuations being superimposed, $u_{i,T}$ is the turbulent field at the inlet prior to mass flux correction, $U_{b,T}$ is the mass flux normalising coefficient, S is the surface area of the inlet and $U_{n,T}$ is the velocity on one cell face on the inlet.

Despite this correction the pressure results were still not entirely accurate and this would appear to be because of the initial interaction between the turbulent fluctuations and the wall boundary condition in the jet impingement region. The reason for this is not definitively known, though there are a number of hypotheses. One such hypothesis is that it is possible a pressure wave is reflected back from the boundary to the inlet plane, where it then interacts with the high pressure region around the inlet and then transports these additional interactions downstream of the inlet.

The reason for this line of thought is that the first overestimation of the pressure occurs at *twice* the time it would take the velocity to travel from the inlet to the ground plane. Further evidence for this conjecture is that the same modelling approach was used to simulate flow in an open channel with the same mesh density and with no jet impingement region. In this case, the pressure fluctuations are *not* observed to increase, as illustrated in Figure 7 and remain low for the duration of the simulation with no evidence of the large pressure fluctuations seen in the impinging jet case. This indicates that the synthetic turbulence model and mass correction have no major errors in the computational approach, but there is some aspect of the impinging jet case that influences

16
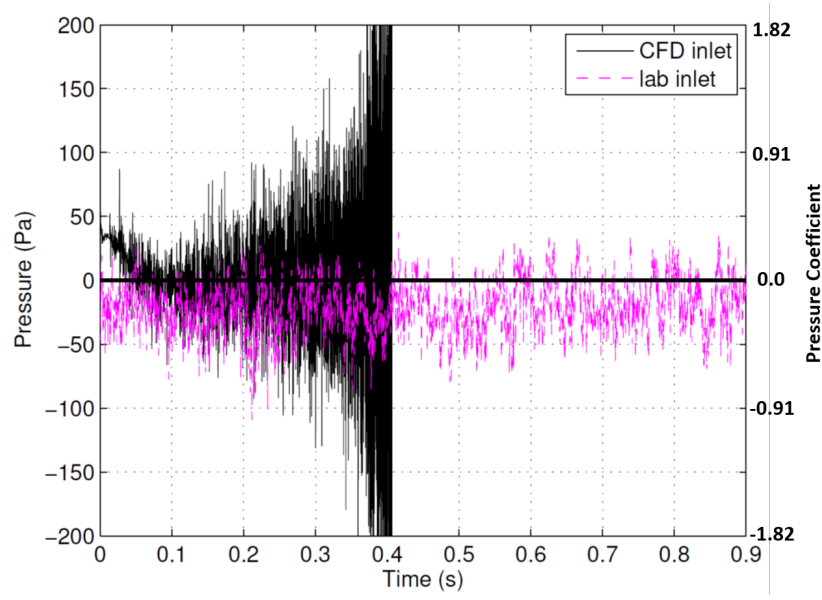
(a) Pressure fluctuations, divergence free
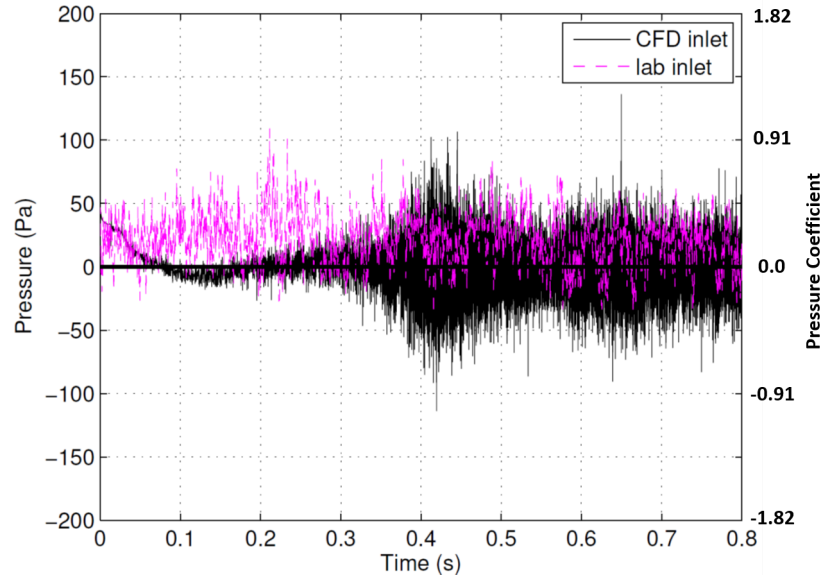
(b) Pressure fluctuations, divergence free, mass flux corrected

Figure 6: The divergence free and mass flux corrected pressure fields at a distance $0.5\,m$ from the jet inlet. The simulation was only run to $0.4\,s$ for the divergence free case as the large pressure fluctuations caused an excessive run time and considering the obvious problem it was unnecessary to run for longer.

17

the model and for this reason, it was decided to continue with this approach. Additionally, in the impinging jet cases, after the initial large pressure fluctuations at inlet, the effect does not appear to be transported further downstream of the impingement region (Figure 8). In the regions of the flow of interest in this investigation, particularly the impinging flow and formation of the primary vortex, along with its interaction with the building structure, it appears that the dominant feature is the primary vortex, and as indicated above, the pressure fluctuations seem to have minimal effect on the results. This is illustrated in Figure 8 but also in a more extensive set of results presented in Haines and Taylor (2018) where good agreement between simulations and the experimental results are demonstrated. A further potential solution to the problems has been identified, which may be to apply the turbulent inlet developed by Yu and Bai (2014). This is because the solution has been mathematically proved to be completely divergence free regardless of the size of turbulent vortices produced / inlet size. However, this requires additional coding and testing and is outside the scope of the current investigation.
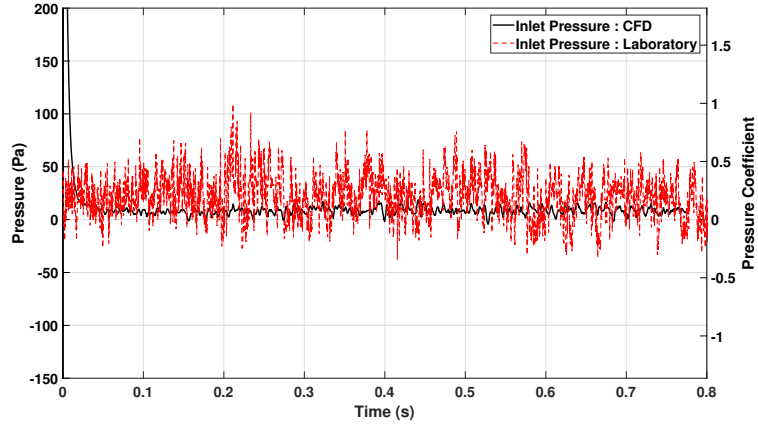
Figure 7: The pressure fluctuations in the centre of an open channel at $\frac{X}{D} = 0.5$.
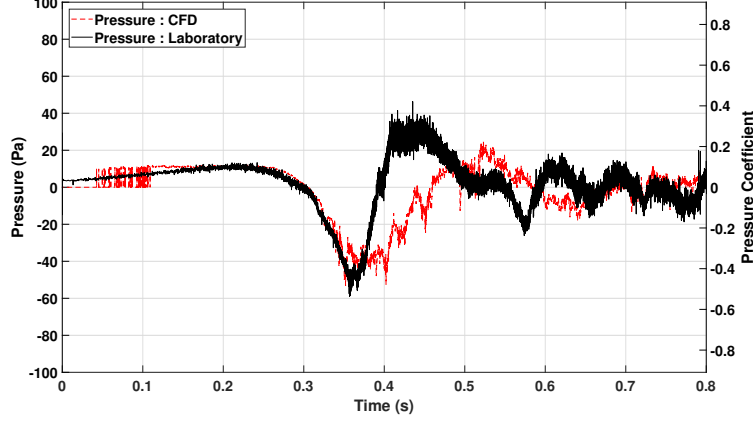
18

Figure 8: The pressure fluctuations at $\frac{X}{D} = 1.0$ at a height of $\frac{Z}{D} = 0.03$.

2.2. Choice of turbulence models and details

Four turbulence models were used to investigate the impinging flow field : the standard OpenFOAM Spalart Allmaras IDDES solver; the standard Open-FOAM Smagorinsky LES model; the dynamic Smagorinsky-Lilly LES model; and a custom $k - \omega$ SST SAS model based on the latest version of this turbulence model by Egorov and Menter (2007). The wall boundary condition for the subgrid-scale viscosity was set as the OpenFOAM wall function, nu-tUWallFunction, for the IDDES and LES turbulence models as the Y^+ value was greater than 1, so small scale turbulence features were not being correctly resolved. For the $k - \omega$ SST SAS model a zero-gradient condition was used as the LES model would only be initiated in the wall region if the Y^+ value was low enough. For the turbulent kinetic energy k and specific dissipation, ω, a wall function was used (the OpenFOAM wall function "kqRWallFunction"). In all of the simulations the kinematic viscosity was set to that of air at $300\,K$ $(1.568 \times 10^{-5}\,m^2 s^{-1})$.

The advantages of LES models over the existing RANS turbulence models of impinging jet flow are that they resolve the turbulent features of the flow in both space and time down to a specific length scale. Any turbulent features below

19

this length scale are filtered out and need to be modelled because of the closure problem, with the standard approach being the Smagorinsky turbulence model proposed by Lilly et al. (1967). A more appropriate model for the impinging jet flow is the dynamic Smagorinsky-Lilly model developed by Lilly (1992) based on work by Germano et al. (1991) which allows the value of the Smagorinsky coefficient, c_s, (Lilly, 1992) to alter across the different resolved length scales and be self consistent across the range of resolved and unresolved scales.

In addition to the pure LES simulations, the $k - \omega$ SST SAS and IDDES models were used within two blended RANS-LES approaches (Gritskevich et al., 2012). Firstly, an improved URANS approach that allows the LES simulation to fall back on the RANS turbulence models in regions where the grid is too coarse, in this case the $k - \omega$ SST SAS model is applied (Menter and Egorov, 2010) and was chosen as Mason et al. (2007) found it to be the best suited of the RANS turbulence models to simulating impinging jets. Secondly the detached eddy simulations (DES) where the switching mechanism is based on the local grid spacing and turbulent length scale of the flow in that region and the Spalart Almaras (Spalart et al., 1997) IDDES model of Shur et al. (2008).

The switching between the LES and RANS models in the $k - \omega$ SST RANS model is governed by the von Karman length scale formula given in equation (7).

$$L_{vk} = \frac{\kappa S}{|u''|} \tag{7}$$

where L_{vk} is the von Karman length scale, based on the traditional version for the atmospheric boundary layer (von Karman and Howarth, 1938), κ is the von Karman constant and has the value 0.41, S is the scalar invariant of the strain rate tensor, given by $\sqrt{2S_{ij}S_{ij}}$ and u'' is the derivative of the u component of velocity in the X direction (Figure 3). (Note that the u and v components on average may be considered symmetrical due to the radial outflow of the vortex.)

The IDDES approach is an improvement over the original DES model of Spalart et al. (1997) and also the DDES model of Spalart et al. (2006) . It is

20

less likely to remain stuck in one of either LES or RANS modes if the wall region mesh density is ambiguous and it is also able to switch regimes if unsteady flow situations arise, such as from a turbulent inlet or obstacle in the flow like a wall mounted cube. Both being key in the flow being studied in this investigation. The switch between the RANS and turbulence model is governed by equation (8).

$$F_{IDDES} = \frac{l_{RANS}}{l_{IDDES}} \tag{8}$$

where F_{IDDES} is based on the RANS turbulent length scale and LES grid length scale. RANS turbulent length scale, l_{RANS}, is determined throughout the computational domain (9) using local values of turbulent energy, k, and specific turbulent dissipation rate, ω (10). At the jet inlet, initial values of $k = 0.19$ and $\omega = 1.78$ are applied.

$$\omega = \frac{\sqrt{k}}{l_{RANS}} \tag{9}$$

$$k = \frac{3}{2} (UI)^2, \qquad \omega = C_\mu^{-0.25} \frac{\sqrt{k}}{l} \tag{10}$$

where U is the mean flow velocity, I is the turbulence intensity, l is the turbulent length scale and C_μ is a turbulence model constant with a value of 0.09.

The LES integral length scale is determined using the approach presented by Gritskevich et al. (2012), where the *IDDES* length scale is given by

$$l_{IDDES} = \tilde{f}_d (1 + f_e) .l_{RANS} + \left(1 - \tilde{f}_d\right) .l_{LES} \tag{11}$$

where

$$l_{LES} = C_{DES}\Delta \tag{12}$$

where $\tilde{f}_d$ is a blending function, and f_e is an elevating function (Gritskevich et al., 2012). Also, C_{DES} and the LES length scale, Δ, are defined as

$$C_{DES} = C_{DES1}.F_1 + C_{DES2} (1 - F_1) \tag{13}$$

$$\Delta = \min \{C_w \max [d_w , h_{max}] , h_{max}\} \tag{14}$$

21

F_1 is an SST blending function, d_w is the distance to the nearest wall, h_{max} is the maximum cell edge length inside the wall boundary layer, and the constants are defined as $C_w = 0.15$, $C_{DES1} = 0.78$ and $C_{DES2} = 0.61$ (Gritskevich et al., 2012).

2.3. Data analysis methodology

For each experimental dataset, ten individual runs were performed and post-processed to provide an ensemble averaged dataset. However, there was significant run to run variation making the choice of which run to compare with difficult. The turbulence properties for an individual run could be used for the simulations, but due to the run to run variation, the question remained as to which of the runs should be selected or was most appropriate for comparison. Likewise, the ensemble average turbulence statistics could be used as input, but this is also problematic as the averaging had the effect of smoothing out many of the larger variations within the impinging flow field. Different experimental runs were used to obtain the jet inlet data and the velocity and pressure results at other locations and for the buildings. As a result, it is unlikely that the average turbulence statistics for the inlet will produce the same "averaged" results at other locations, and due to the run to run variation of the experiment, is not easy to check if this would be the case. Hence, turbulent statistics from an individual run and the ensemble average were both used in separate simulations, to investigate what effect the turbulence properties had on the flow. For the simulations presented herein, the turbulence intensity at jet inlet for the "ensemble average" case was 0.0884 and for the "individual" case was 0.225. At the location $0.5m$ below the inlet, these gave turbulence intensities of respectively 0.0533 and 0.155 which compare to the values measured in the laboratory experiment of 0.0509 for the "ensemble average" and 0.163 for the "individual" case.

Similarly, when comparing results with measured time histories of velocity or pressure coefficient, the run to run variation in the experiment complicates the choice of which dataset to compare to. Depending which individual dataset

22

run was used, either good or poor agreement between the simulations and the data could be demonstrated and comparing with the ensemble average data is also not ideal due to the smoothing effect of the averaging process. As used in Haines and Taylor (2018), for time histories, simulations were compared with the ensemble average dataset and the upper and lower limits of the experimental data were indicated to provide bounds for the results.

With the large amount of data being produced it was impractical to display every graph to allow a comparison between the various turbulence models, mesh densities and the laboratory data set. To provide a summary of the results, for key measurement points a time series of differences between the laboratory and CFD results at each location (equation (15)) was determined, and the mean (equation (16)) and standard deviation (equation (17)) of the difference time series was calculated. A low value of the mean meant the average of the signal was close to the experimental value (although turbulent fluctuations may still differ) and a low standard deviation indicated that the turbulent fluctuations were similar. If both were low it indicated a good fit between the two signals.

$$diff(t) = Lab(t) - CFD(t) \tag{15}$$

where $Lab(t)$ is the time series of the laboratory data at a specific location and $CFD(t)$ is the time series of the CFD data at the corresponding location. The time series can be for either velocity or pressure.

$$mean_{difference} = \overline{|diff(t)|} \tag{16}$$

$$\sigma_{difference} = \sigma(diff(t)) \tag{17}$$

These results were then presented on a graph, displaying both the mean and standard deviation, of which an example is given in Figure 12. The bars represent the mean (equation (16)) of each turbulence model or mesh density and the standard deviation (equation (17)) is represented by the markers on the graph. For figures of this type labelled "velocity" the statistics presented

are determined from the predicted velocity time history for the simulation in question, and similarly the label "pressure coefficient" refers to statistics from time histories of pressure coefficient.

3. Results and discussion

3.1. Turbulence model comparisons

As highlighted earlier, the comparison of the four turbulence models used a mesh of ≈ 15.4 million cells with a freestream cell size of $20\,mm$. A mesh sensitivity investigation is later considered on the final selected turbulence scheme.

Inlet Flow.
Figure 9 illustrates the velocity time history $0.5\,m$ below the jet inlet for the individual run turbulence levels for all CFD models compared to the ensemble average from the simulator data. As indicated earlier and for clarity, the CFD mesh cell size in this region is the same as the free stream cell size at $20\,mm$. From this it is immediately apparent that the two turbulence models which were best at capturing the laboratory turbulence in the inlet region were the two LES simulations, the dynamic Smagorinsky and Smagorinsky. While the differences were smaller for the ensemble level of turbulence, illustrated in Figure 10 it is still apparent that the two LES models outperform the others. The power spectral density (Figure 11), shown for individual run turbulence levels only, also indicate that the two LES simulations perform the best, although all models do show slightly higher energy at the lower frequencies [5]. These results are also backed up by the mean and standard deviation differences for the inlet region, Figure 12.

It would also appear from Figures 9-11 that the IDDES approach is not operating as a pure LES simulation below the inlet, given the lack of fluctuations and smooth transitions between velocities. The $k - \omega$ SST-SAS model

---

[5]For the power spectral density, the results were processed using standard fft functions in Matlab2017b and filtered using a "rectangular" window.

also exhibits similar behaviour and is much smoother than the two LES models, perhaps suggesting it is not remaining in the LES regime at all times and is switching between the schemes (with the switching parameter being the turbulent length scale) depending on the velocity produced by the turbulent inlet. However, this conjecture has not been determined explicitly.
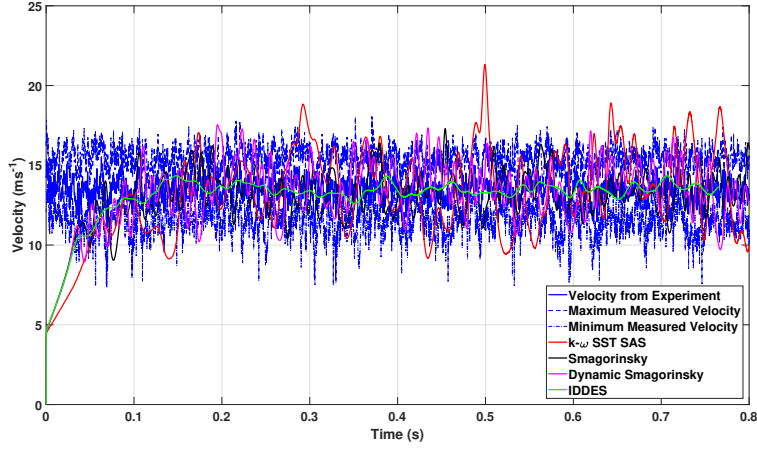
Figure 9: A velocity time history comparison between the laboratory simulator experimental data and the CFD simulation $0.5\,m$ below the inlet region using individual run turbulence levels.

In addition the $k - \omega$ SST-SAS model also had issues in supporting the turbulent velocity fluctuations without also producing excessive pressure fluctuations, which are illustrated in Figure 14. Reducing the turbulence at the inlet to the ensemble levels resolved this issue, as illustrated in Figure 15. The IDDES simulation had an alternative problem, with the simulation becoming unstable more rapidly for the ensemble turbulence levels. For clarity, the range of pressure coefficient variation (maximum and minimum values) are indicated separately in Figure 13 rather than in the comparisons with the CFD results.

Impinging Jet Flow.
It was also interesting to examine how the turbulence models performed downstream of the inlet condition, especially considering two of the models had issues
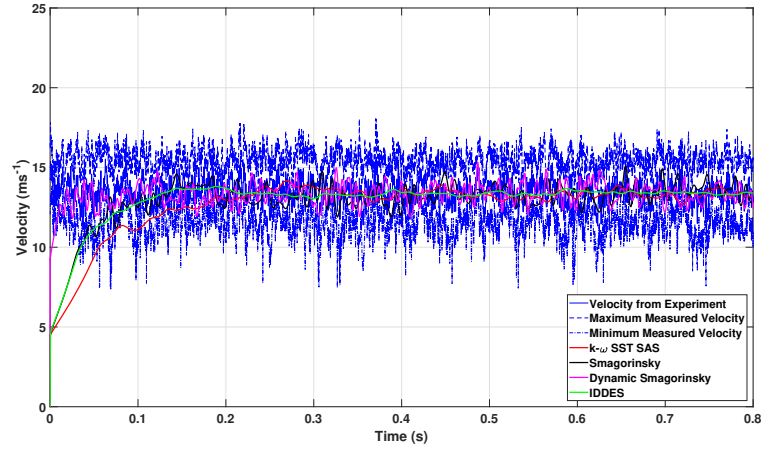
Figure 10: A velocity time history comparison between the laboratory simulator experimental data and the CFD simulation $0.5\,m$ below the inlet region using ensemble average turbulence levels.
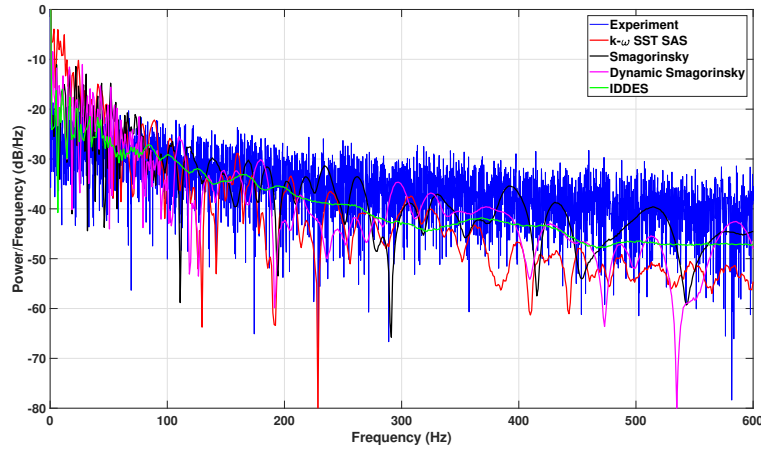
Figure 11: A comparison of the power spectral density of the experimentally measured and simulated velocity $0.5\,m$ below the inlet region (individual run turbulence levels).
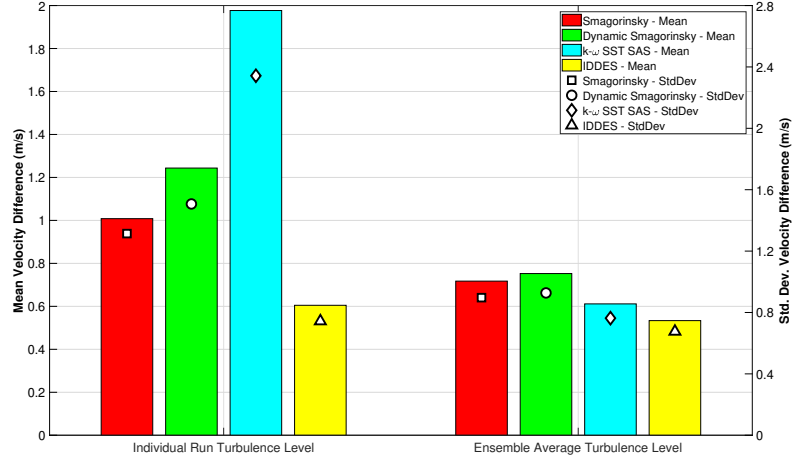
(a) Velocity
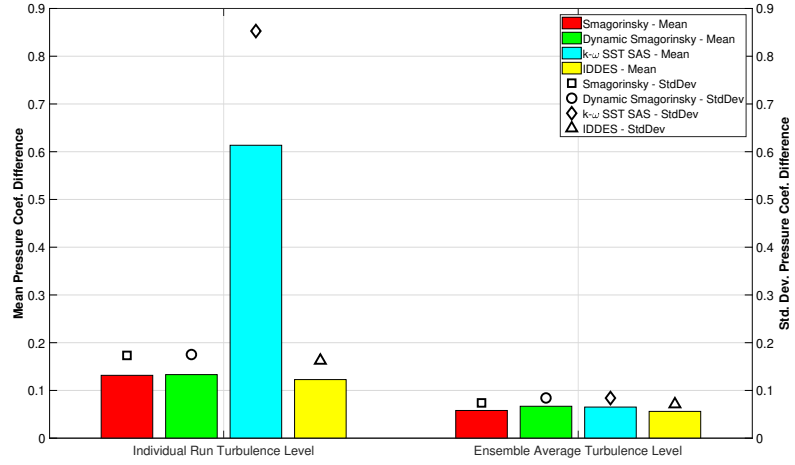
(b) Pressure Coefficient

Figure 12: The performance of the turbulence models $0.5\,m$ below the inlet jet for the individual and ensemble run turbulence levels at the inlet.
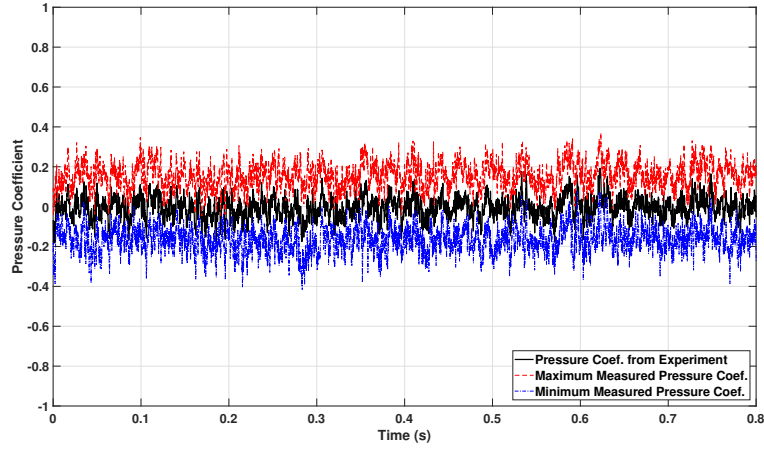
Figure 13: Ensemble average of measured pressure coefficient time history along with minimum and maximum values from individual runs at $0.5\,m$ below the inlet region.
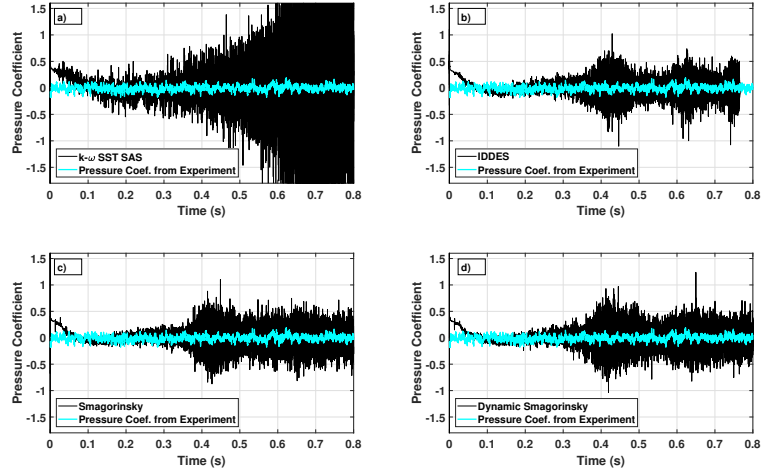
Figure 14: A pressure coefficient time history comparison between the laboratory simulator and the CFD simulation $0.5\,m$ below the inlet region using individual run turbulence level.
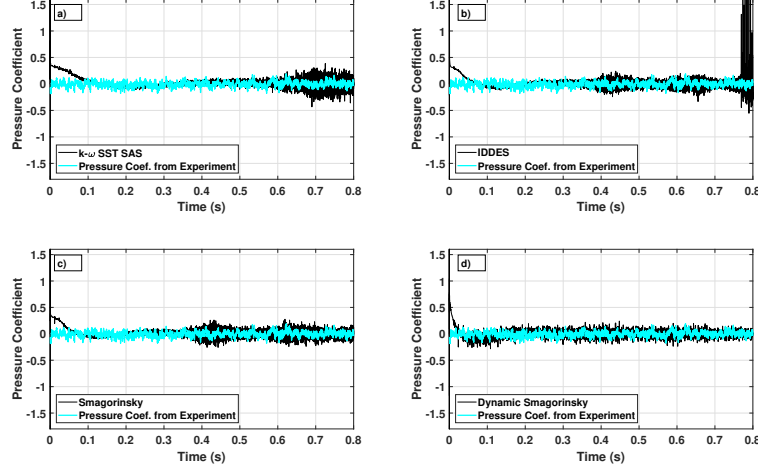
Figure 15: A pressure coefficient time history comparison between the laboratory simulator and the CFD simulation $0.5\,m$ below the inlet region using ensemble average turbulence level.

in capturing the turbulence properties at the inlet. Four distances from the centre of impingement were examined, consistent with the measurement locations used in Jesson et al. (2015) with all measurements being taken down the centreline of the jet at a height of $\frac{Z}{D} = 0.03$ (the height at which the maximum velocity occurred in the simulation): $\frac{X}{D} = 1.0$, $\frac{X}{D} = 1.5$, $\frac{X}{D} = 2.0$ and $\frac{X}{D} = 2.5$. For each of these locations a velocity time, pressure time and velocity height profile was produced and compared to the laboratory data.

The velocity time history at $\frac{X}{D} = 1.5$ (Figures 16 and 17) showed that the two LES turbulence models gave the best fit, and in general the CFD tended to overestimate the peak velocity. This is even when compared to the highest velocities recorded from an individual run, which is illustrated on the figure by the narrower blue lines[6]. The ensemble turbulence run had an even greater peak velocity. This was because in the individual run turbulence case the primary

---

[6]The experimental results for an individual run are shown by the solid blue line. The narrower blue lines either side of the experiment show the maximum and minimum results from the set of 10 runs.

vortex decayed more rapidly because of the presence of the turbulent fluctuations. This assessment of the results at $\frac{X}{D} = 1.5$ was also confirmed by the mean and standard deviation of differences given by Figure 18. However, these fits also show that for the velocity time profiles results became worse further from the inlet.
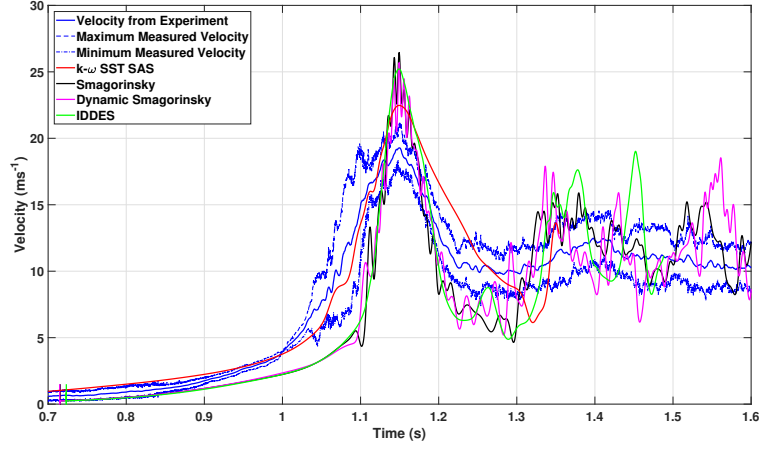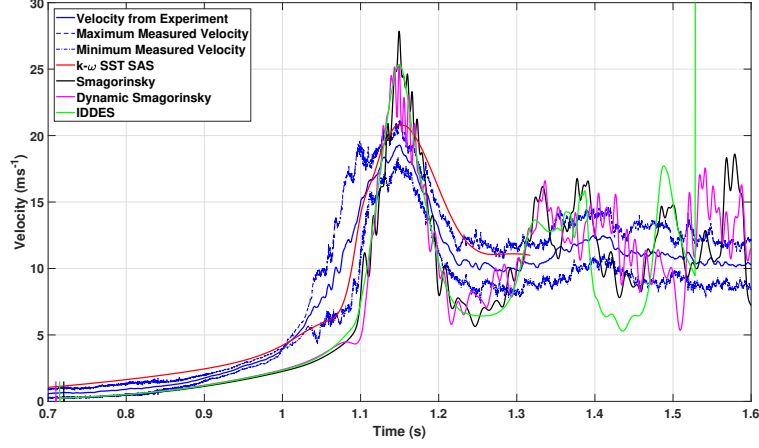

Figure 16: A velocity time history for the four turbulence models at a location of $\frac{X}{D} = 1.5$ for the *individual* run turbulence level.

Also from Figure 16 there is a clear a difference in the duration of the primary peak, identifiable from the narrower / sharper peaks in the CFD results. To investigate the cause of the poor fit further from the centre of impingement and the sharper primary peak the flow was visualised, the vortex development examined and vortex translation velocity was calculated. "Vortex translation velocity" in this context refers to the velocity radially outwards from the jet centre along the ground plane, of the primary vortex in the vortex ring structure formed when the jet impinges on the ground plane (Haines and Taylor, 2018). The cause of the poor fit and sharper pressure / velocity primary peaks immediately becomes apparent from the vortex velocities illustrated in Figure 19. The laboratory measured data for translation velocity is determined from analysis of flow visualisation of the experimental rig by assessing the video footage of the
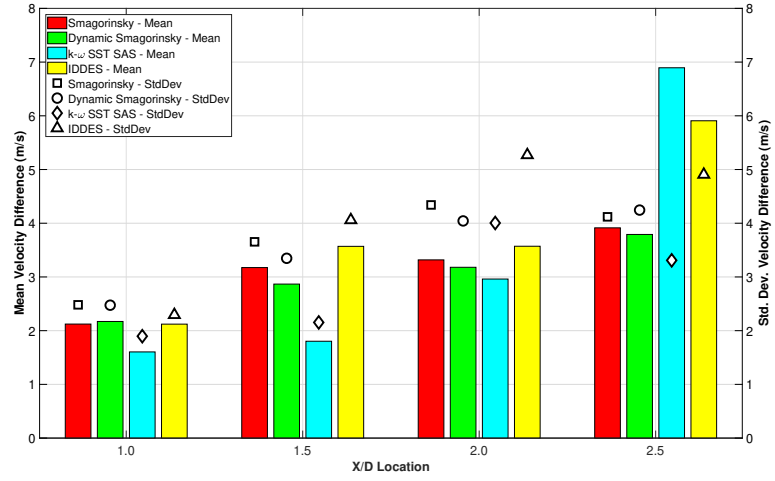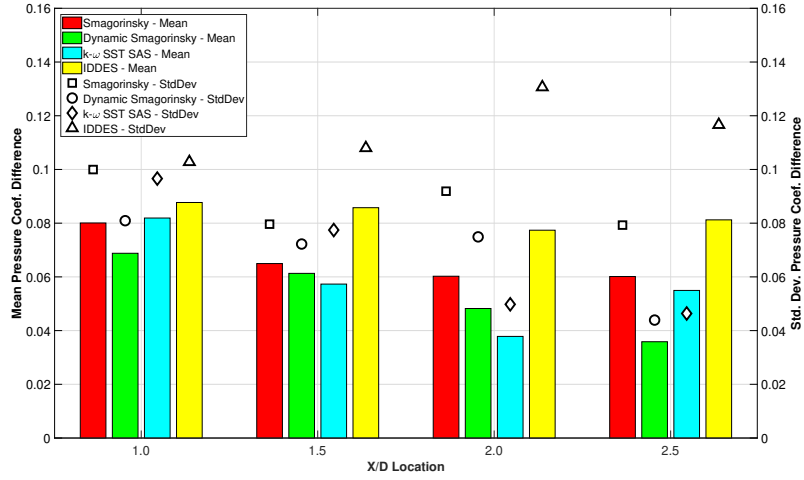
Figure 17: A velocity time history for the four turbulence models at a location of $\frac{X}{D} = 1.5$ for the *ensemble average* turbulence level.

results (McConville et al., 2009; Haines, 2014). The calculation of the translation speed involved an assessment of the differences between the captured flow fields on consecutive frames of videos of the flow visualisation and the upper and lower bounds illustrated in Figure 19 are due to the errors arising from the process (equivalent to approximately $\pm 0.2 m/s$ or $\pm 6.5\%$). In Figure 19, the vortex velocities are considerably higher than the laboratory simulations for the LES turbulence models and IDDES, resulting in a shorter duration primary peak as the vortex is travelling faster. The reason the $k - \omega$ SST SAS model has the correct duration peak is because it has the closest vortex translation velocity to the laboratory simulation. It is noted that the results of the IDDES model become unstable towards the end of the simulation in Figure 17. From investigating the results, it is most likely (though not conclusively shown) that this is due to the switching from RANS to LES models used in the hybrid approach close to the wall (Section 2.2), and in some cases a similar feature was exhibited in the $k - \omega$ SST-SAS model.

There are a number of possible reasons for the translation velocity difference between the CFD and laboratory simulations. As indicated in Section 2, the

31

(a) Velocity

(b) Pressure Coefficient

Figure 18: The performance of the turbulence models for the individual turbulence inlet condition in producing the correct velocity and pressure time histories at the four $\frac{X}{D}$ locations.
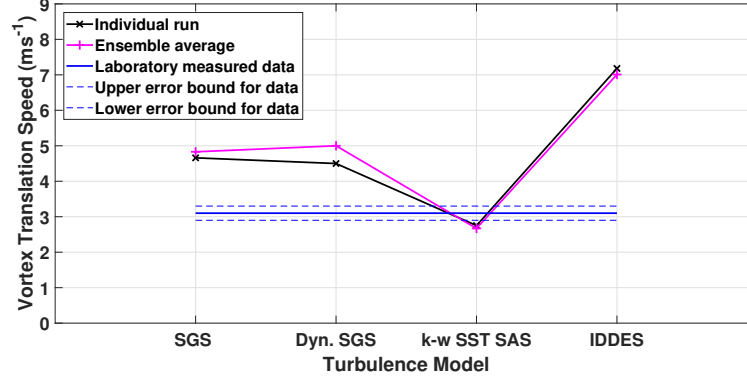
Figure 19: The variation of vortex translation velocity with turbulence model and turbulent settings at the inlet.

different jet generation mechanism in the experiment and the CFD simulations may be a contributing factor. It was felt that the air flow from the flaps as they dropped during opening may have affected the vortex formation in the experiment, thus affecting the size of the primary vortex or affecting its rate of decay which would explain the increased velocity in the CFD simulation. As these aspects were not measured in the experiments, the exact effect of the flaps on the flow field is not known. It was felt that the complexity of modelling these flaps in the simulation would lead to excessive computational cost and would not provide significant improvements to the simulations bearing in mind the unknowns and the run to run variation from the experiment. Instead it was more practicable to just note the differences between CFD and experiment and account for these differences when analysing and interpreting the simulations. The effect of the translation velocity difference on the flow field and how this affects the velocity and pressure distribution on low rise structures is discussed in more detail in Haines and Taylor (2018).

Despite these differences between experiment and CFD modelling, there are also issues with the turbulence models. In the $k - \omega$ SST SAS the vortex appeared to be travelling through a more viscous fluid (it hadn't reached the $\frac{X}{D} = 2.5$ location after $1\,s$ as it had decayed), while the IDDES turbulence model

had the opposite issue. The similar translation velocity between the individual run inlet turbulence and ensemble inlet turbulence would also suggest that the two hybrid RANS-LES models are not currently capturing the turbulence at the inlet correctly.

The two LES models performed better in this regard, the higher inlet turbulence caused the primary vortex to decay more rapidly than the ensemble turbulence case, hence have a lower translation velocity. The primary vortex also matched how the vortex developed in the laboratory, despite travelling more rapidly. This might either be because of the physical differences between the simulations or an issue in the turbulent mixing in the LES turbulence models, which might be caused by the relatively coarse mesh used.

Velocity Height Profiles.
The vortex translation velocity also caused an issue with the velocity height profiles, illustrated at the $\frac{X}{D} = 1.5$ location in Figure 20 for both the individual run and ensemble average turbulence levels. The data presented in Figure 20 is the *maximum* velocity measured or predicted at this location, i.e. the maximum velocity from the time histories. While the general shape of the profiles and height of maximum velocity were correct, the maximum velocities were overestimated. Figure 21 illustrates the mean and standard deviation of the differences between simulations and experiment (Section 2.3), with the differences between results at each height being considered in this case. The results indicate that the further the measurement was taken from the centre of impingement the worse this issue became, with the fit of the mean increasing with $\frac{X}{D}$ for three of the turbulence models,

Of all the turbulence models it was the k-ω SST SAS which performed marginally better than the other three, which had similar performance levels. Even the k-ω SST SAS overestimated the velocity height profile because of the slightly higher vortex translation velocity and at a distance of $\frac{X}{D} = 2.5$ it heavily underestimated the velocity as the vortex had decayed by this location.
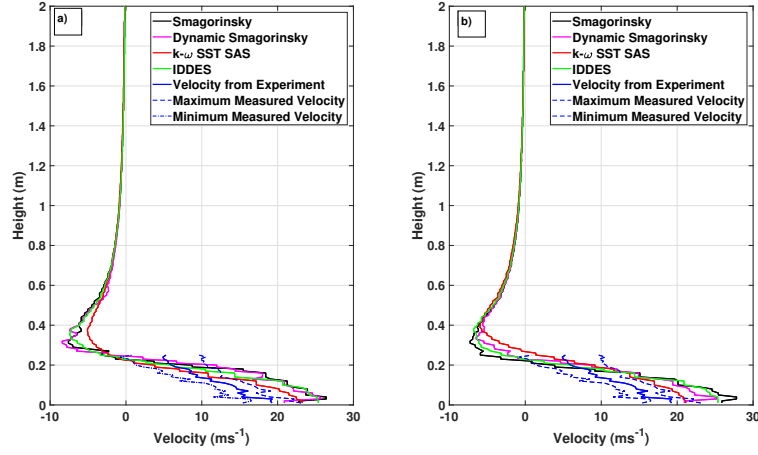
34

Figure 20: A maximum velocity with height profile for the four turbulence models at a location of $\frac{X}{D} = 1.5$. (a) Individual run turbulence level; (b) Ensemble average turbulence level
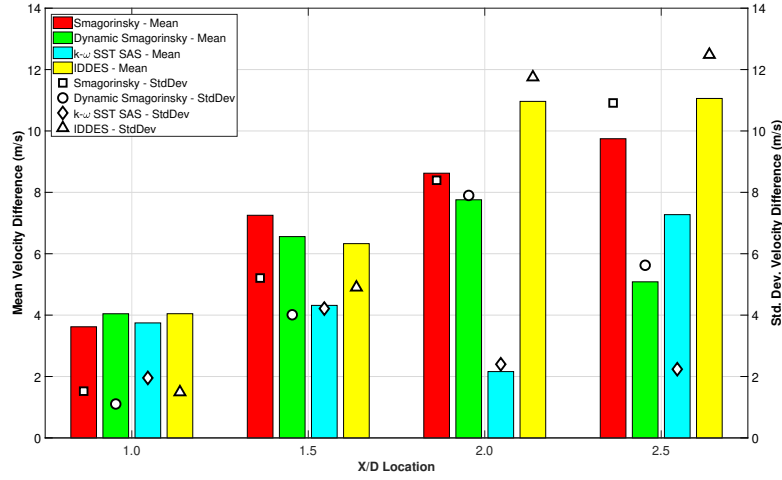

Figure 21: The performance of the turbulence models in capturing the correct velocity height profile fit for the individual turbulence level .

Pressure on Building Faces.

The final and perhaps most important region from a wind engineering point of view and for this investigation was the performance of the CFD models in capturing the pressures around the model cube building. As highlighted in Section 2, a cube model building, side length $60\,mm$, was included in the flow on the ground plane at location $\frac{X}{D} = 1.5$, $\frac{Y}{D} = 0.0$ (Figure 3a). The pressure results considered in this section is located at the *centre* of each face, and a more detailed analysis and wider range of pressure data is considered in Jesson et al. (2015) and Haines and Taylor (2018).

Firstly examining the pressures on the centre tap of the front face of the cube, Figures 22 and 23 for the individual run and ensemble average turbulence model respectively, revealed that the slightly excessive pressure fluctuations had mixed out for all but the k-ω SST SAS turbulence model by the time they reached the building. The IDDES model had a stability issue for both the turbulence levels and also overestimated the pressure fluctuations after the primary vortex had passed.

The Smagorinsky and dynamic Smagorinsky again performed well, although the Smagorinsky was the more unstable model around the building region, with evidence of instabilities beginning to appear towards the end of the pressure time series for the individual run turbulence (Figure 22). Examining the mean and standard deviation differences for the individual run and ensemble turbulence, given by Figure 24, revealed that the fit across each building face was consistent between turbulence models, with the dynamic Smagorinsky performing the best. A much more detailed investigation of the effect of the downburst flow on the pressure distribution and loading on low rise buildings from these simulations is provided in Haines and Taylor (2018). The analysis presented in this previous research includes a summary of particular flow features such as possible vortex shedding, asymmetric flow and conical vortices on the roof, as identified in Jesson et al. (2015). The CFD results are used to understand these features and their effect on the forces on the building along with the implications for wind engineering practitioners.
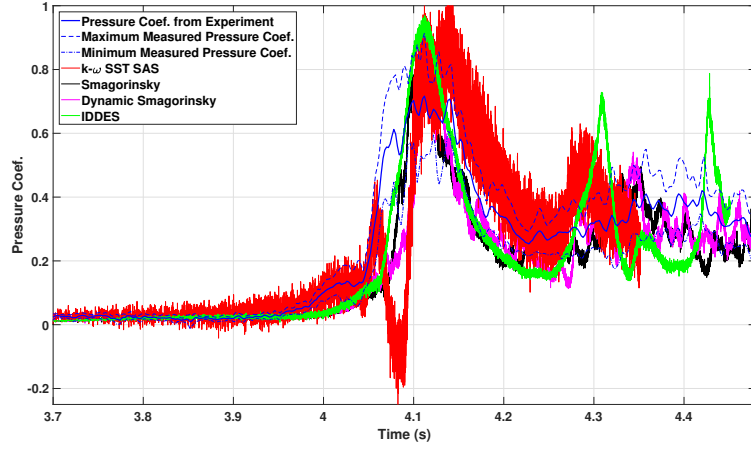
Figure 22: The pressure coefficient time history for the four turbulence models on the front face of the $60\,mm$ model cube building for the individual run turbulence level.
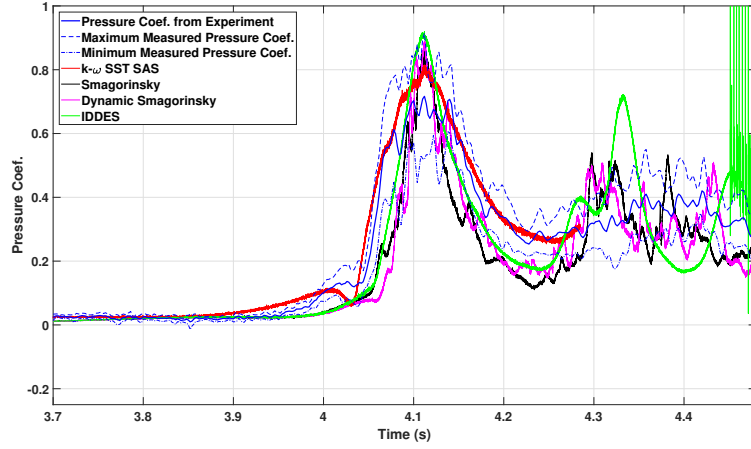

Figure 23: The pressure coefficient time history for the four turbulence models on the front face of the $60\,mm$ model cube building for the ensemble average turbulence level.
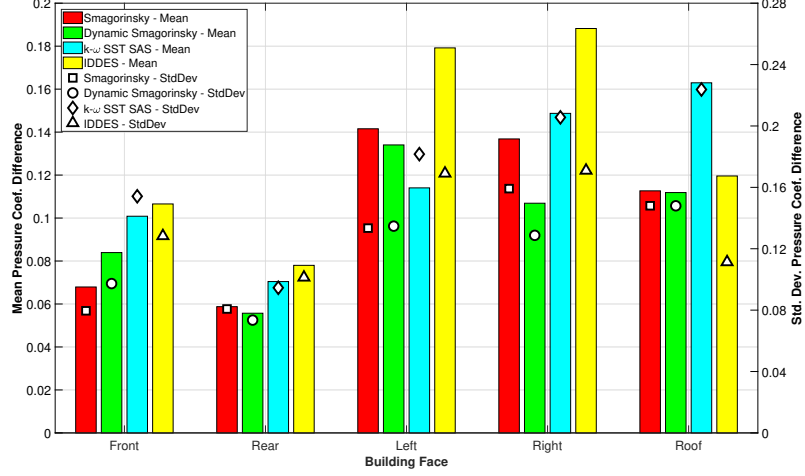
37

Figure 24: The performance of the turbulence models in capturing the pressure coefficients around the cube model building.

The reason for the improved performance for the dynamic Smagorinsky turbulence model is demonstrated in Figure 25, which illustrates the left face pressure tap for the individual run turbulence for the laboratory, dynamic Smagorinsky and Smagorinsky turbulence models. The Smagorinsky turbulence model has not quite captured the flow separation around the cube, resulting in it underestimating the side pressures on the building, hence giving a worse fit with the data.

Summary.

From all of the above it is apparent that of the four turbulence models tested it was the dynamic Smagorinsky which performed best and is selected to continue the remainder of the analyses. This model provided best agreement for the velocity and pressure time histories at the measurement location and generally had the lowest mean and standard deviations of differences. However, it is also worth noting that in order to get the blended LES-RANS approaches working it is likely the mesh would need to be very carefully refined, as detailed in Spalart (2001) and Spalart et al. (2006), to prevent them becoming stuck or
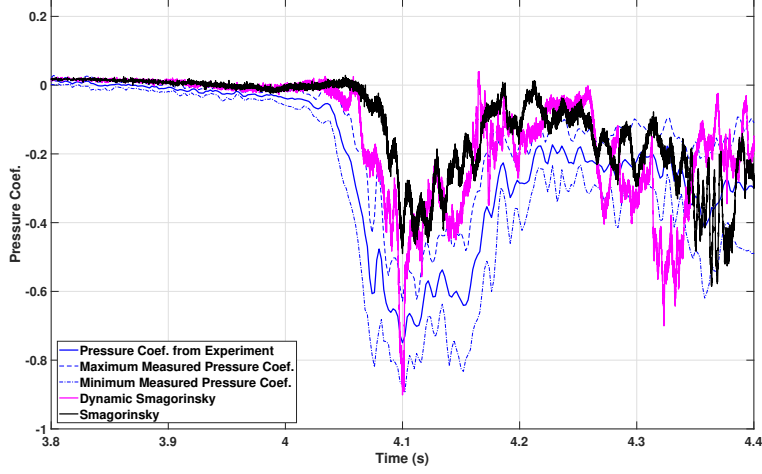
Figure 25: The pressure coefficient time history for the laboratory, Smagorinsky and dynamic Smagorinsky turbulence models on the left face of the $60\,mm$ model cube building for the individual run turbulence level.

fluctuating between the RANS and LES models, which is what was happening to the $k-\omega$ SST SAS model and to a certain extent the IDDES. However, given the dynamic Smagorinsky is to be used for the remaining analyses, refining the mesh of the blended LES-RANS models was deemed unnecessary at this stage. For a complete and thorough investigation, a mesh sensitivity assessment would be undertaken for all four turbulence models, but as the dynamic Smagorinsky is being taken forward and used to assess the downburst effects on structures (Haines and Taylor, 2018), only this model is considered in the following section.

3.2. Mesh density comparisons

Earlier, it was highlighted that the Y^+ values were significantly higher than the usual recommended limits. Running a full LES simulation is not practical for this investigation and this leaves the question as to whether the mesh density is high enough to allow a reasonable LES simulation to be produced, given the use of wall functions. To test this the dynamic Smagorinsky model was run with three different mesh densities, with the same turbulence level at the inlet

39

to see if the results demonstrated small mesh dependency.

For each of the three mesh densities the velocity time histories of the flow $0.5\,m$ below the inlet were compared to the laboratory simulation illustrated in Figure 26. The mean and standard deviation differences are also given in Figure 27. The turbulent inlet has not captured the turbulence properties in exactly the same fashion for each of the mesh densities, but given the lower than ideal cell size and difficulties in producing synthetic turbulence the match is reasonable and comparable.
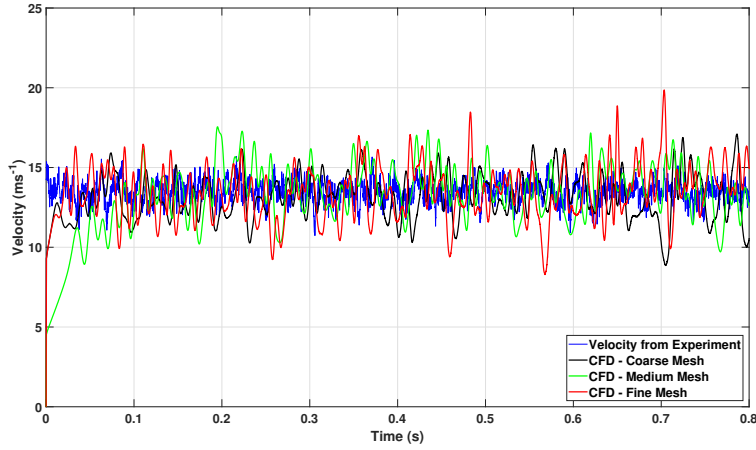
Figure 26: The mesh dependency for the velocity time history of the individual run turbulence $0.5\,m$ below the inlet.

However, these results were complicated by the fact that a change in mesh density altered the pressure fluctuations in the inlet region significantly, which is illustrated in Figure 27 and Figure 28. The cause of these differences are twofold, firstly the coarse mesh cell size does not provide reliable resolution of the turbulent fluctuations. Secondly, the mesh changes also introduced cells of varying aspect ratio at inlet, for both the coarse and fine meshes, that led to numerical instabilities giving the large pressure fluctuations.

To address these two issues the mesh was refined in the inlet region so that the coarse mesh was of sufficient resolution to give reliable modelling of the
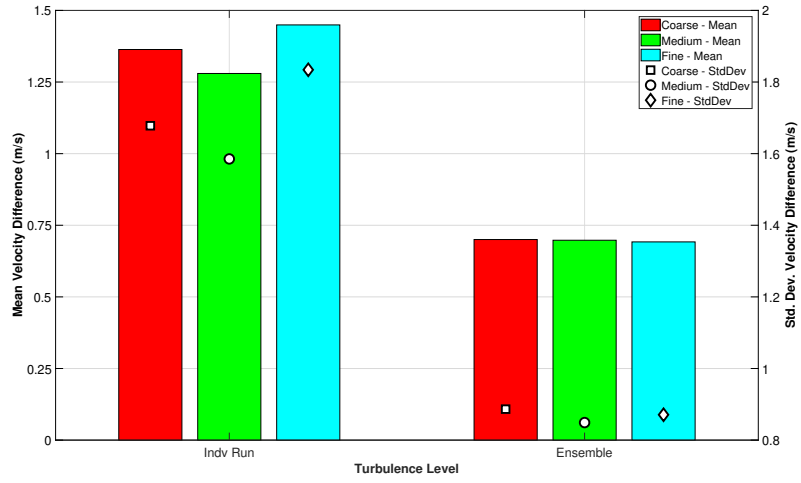
(a) Velocity
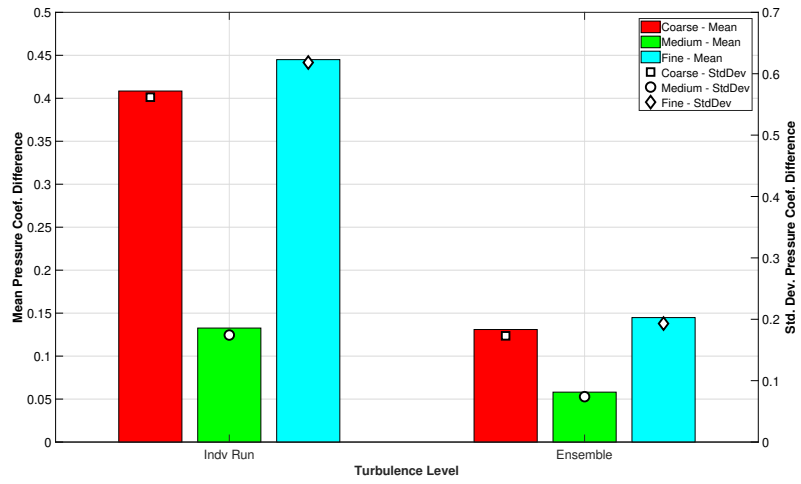
(b) Pressure Coefficient

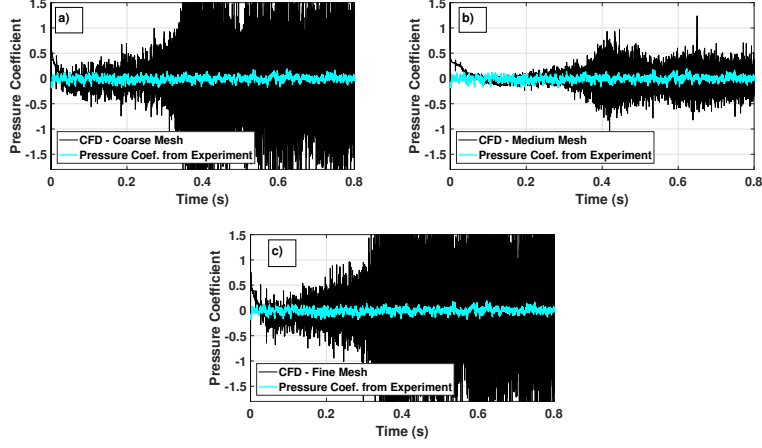Figure 27: The mesh dependency of the dynamic Smagorinsky model, $0.5\,m$ below the inlet.

Figure 28: The mesh dependency for the pressure coefficient time history of the individual run turbulence $0.5, m$ below the inlet.

turbulent fluctuations, and also to as far as possible maintain cells of constant aspect ratio. Similarly the mesh at inlet for the fine mesh was adjusted to ensure constant aspect ratio cells. The nature of the OpenFOAM meshing software meant the easiest way to achieve this yet still have a manageable mesh size was to adjust the domain size from $10 \times 10 \times 2.5\,m$ to $9.8 \times 9.8 \times 2.4\,m$. Refining the mesh increased the number of cells in the mesh from $11,054,940$ to $16,010,456$ for the coarse mesh, from $15,338,950$ to $23,949,473$ for the standard mesh and from $20,154,014$ to $28,370,238$ for the finer mesh. For the simulations to be practical on the facilities available, the mesh refinement close to and around the cube building was modified to reduce the number of cells, but the cells *at* the cube surface were maintained at the same size as the original mesh.

Figures 29, 30 and 34 illustrate that these solutions have reduced the pressure fluctuations but not completely matched them with the laboratory results. The velocity fluctuations were also improved and are illustrated in Figures 31, 33 and 34. The power spectral density (Fig. 32), comparing results from the different mesh densities with the experimental data, also show that the velocity frequency content is still consistent with the measurements. Also, there is consistency with

42

previous results, with the simulations indicating slightly higher energy at the lower frequencies.
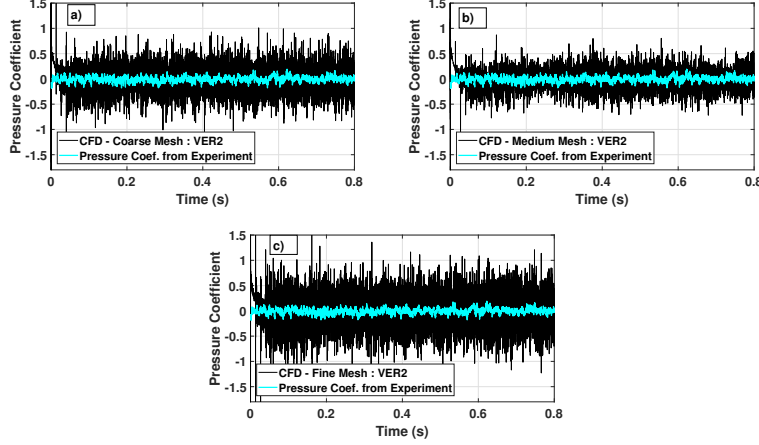

Figure 29: The mesh dependency for the revised mesh for the pressure coefficient time history of the individual run turbulence $0.5\,m$ below the inlet.

With the improvements in the pressure fluctuations in the inlet region the fits were compared for the velocity time, pressure time and velocity height at four locations, $\frac{X}{D} = 1.0$, $\frac{X}{D} = 1.5$, $\frac{X}{D} = 2.0$ and $\frac{X}{D} = 2.5$. Figures 35 and 36 illustrate that the differing mesh densities show no difference at $\frac{X}{D} = 1.5$ for either of the turbulence levels in the peak region and only slight differences in the positioning of fluctuations after the peak region. The mean and standard deviation of differences illustrated in Figure 37 also showed that the fit in other regions was improved over the older mesh which was used in the turbulence model test as the fit in the $\frac{X}{D} = 2.5$ region now matches that of the closer regions. This is because the CFD simulation is now able to support more small scale vortices which appears to have improved the transfer of energy from the larger to smaller scales, reducing the translation velocity of the primary vortex.

However, there are still some issues with the velocity height profiles (Figure 38), though these are consistent with the earlier results. While the mean and standard deviation of differences given by Figure 39 were generally good and
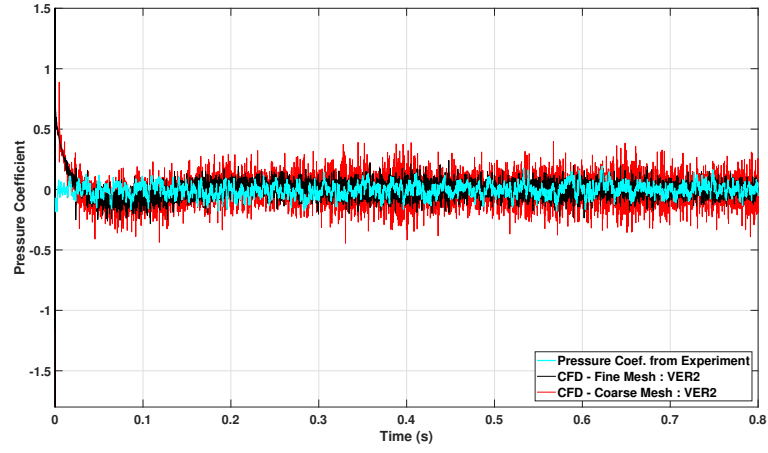
Figure 30: The mesh dependency for the revised mesh for the pressure coefficient time history of the ensemble average turbulence $0.5\,m$ below the inlet.
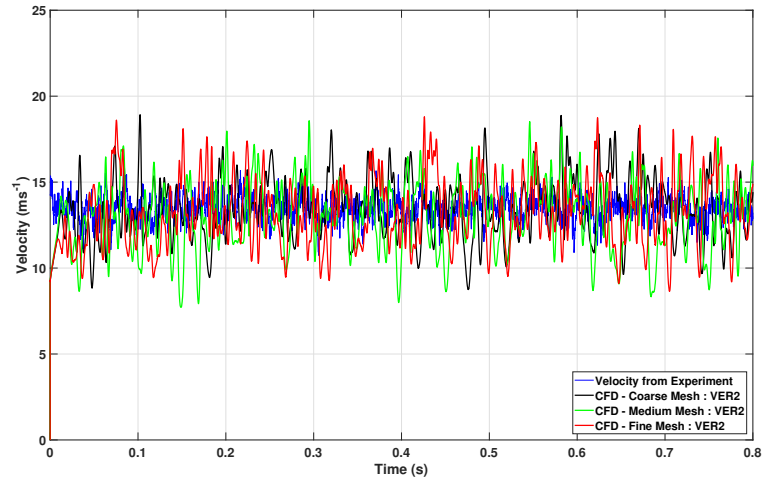

Figure 31: The mesh dependency for the revised mesh for the velocity time history of the individual run turbulence $0.5\,m$ below the inlet.
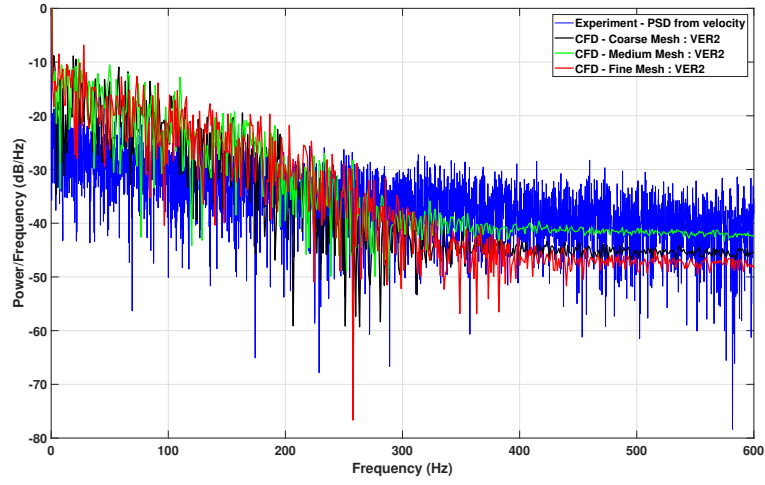
44

Figure 32: A comparison of the spectra of the experimentally measured and simulated velocity $0.5\,m$ below the inlet region : Effect of mesh density.
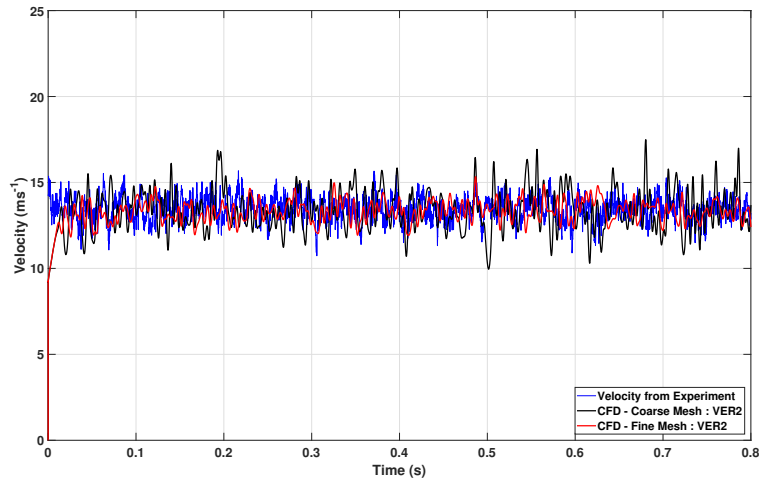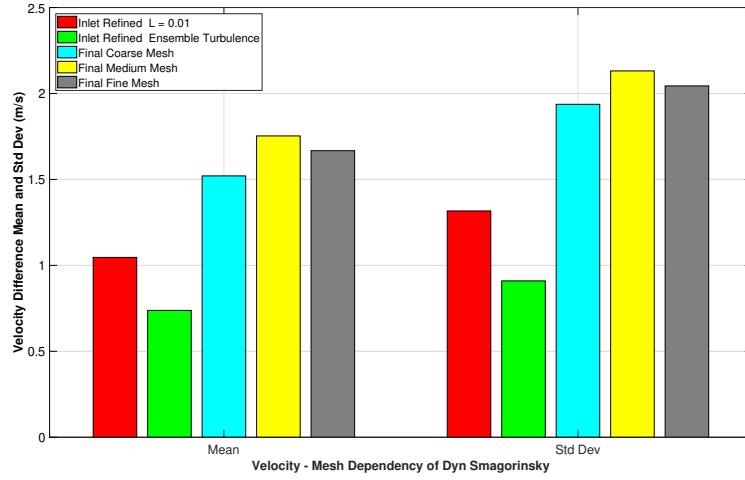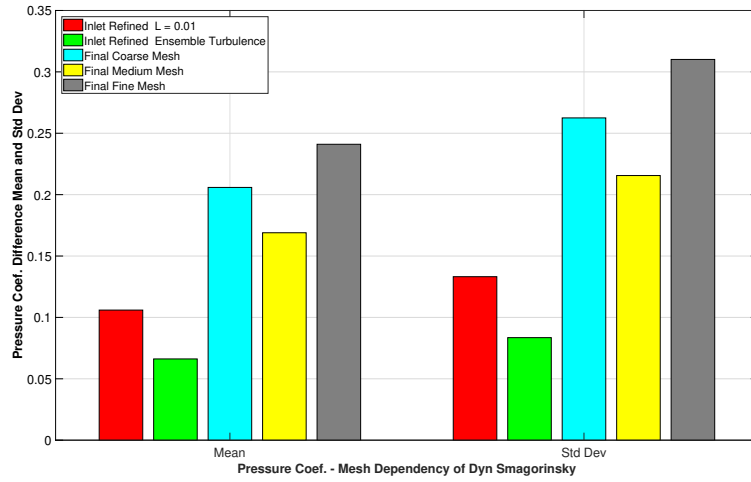

Figure 33: The mesh dependency for the revised mesh for the velocity time history of the ensemble average turbulence $0.5\,m$ below the inlet.

(a) Velocity

(b) Pressure Coefficient

Figure 34: The mesh dependency of the dynamic Smagorinsky model on the revised mesh $0.5\,m$ below the inlet.
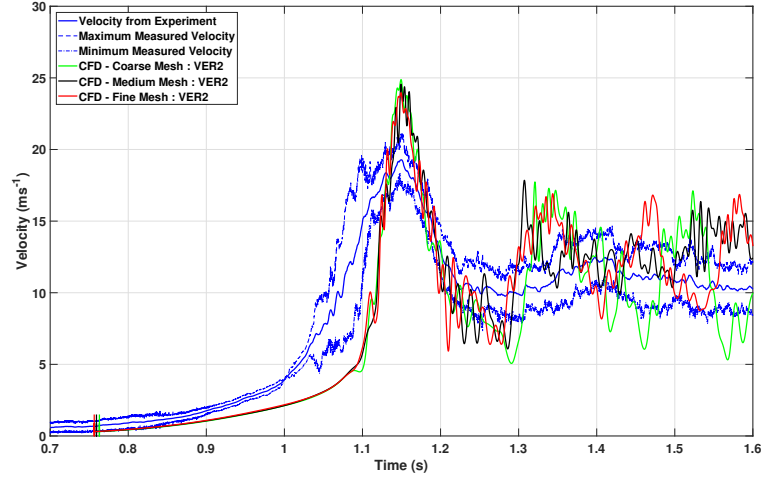
Figure 35: The mesh dependency for the individual run turbulence velocity time history at a location of $\frac{X}{D} = 1.5$.
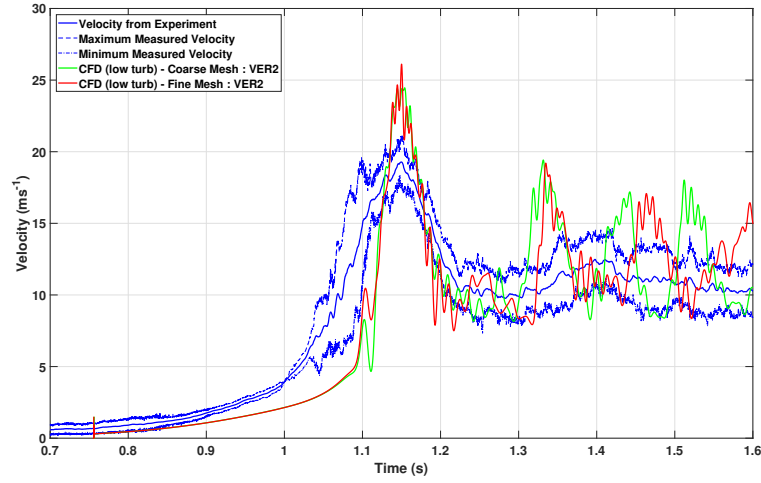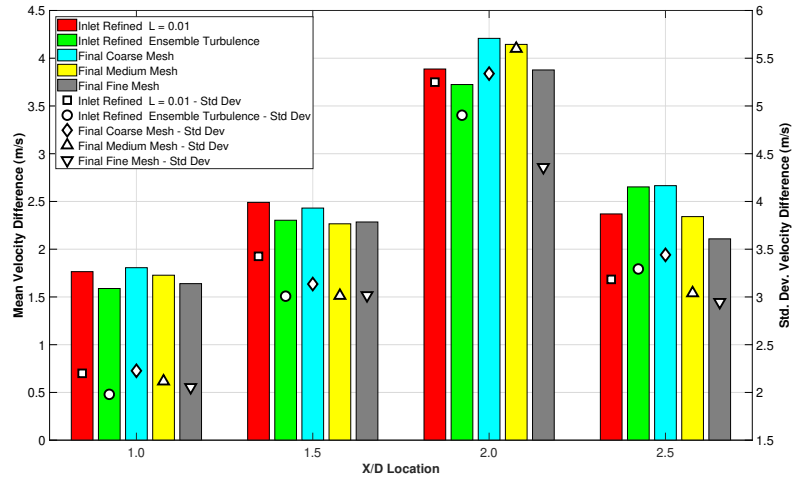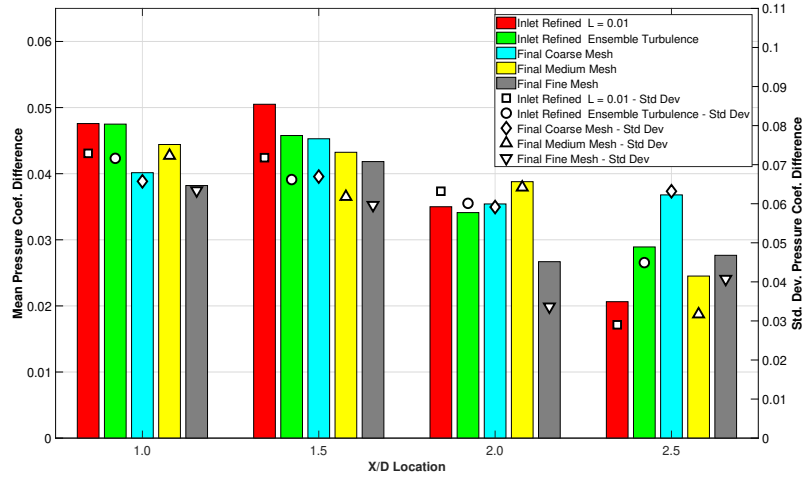

Figure 36: The mesh dependency for the ensemble average turbulence velocity time history at a location of $\frac{X}{D} = 1.5$.

(a) Velocity

(b) Pressure Coefficient

Figure 37: The mesh dependency of the dynamic Smagorinsky model on the revised mesh. Variation of velocity and pressure coefficient with location from centre of jet.

there were very little difference between each of the locations and meshes, there was still an issue with the maximum velocities, especially at low levels. This is clearer in Figure 38 which illustrates the maximum velocity with height profiles for the individual and ensemble average turbulence. Although it is acknowledged that there is limited data at heights above $0.2\,m$ the velocity appears to be coming close to the trend suggested by the laboratory data. However, below this height the velocity is overestimated.

There are two likely causes for this issue. The first is that the surface roughness was not modelled in the CFD simulation, which would result in a higher velocity for the CFD. The second is that the wall modelling functions used close to the ground plane are not capturing the velocities correctly. The only solution to this issue would be to run a wall resolved LES simulation, which is not practical with current computing capabilities.
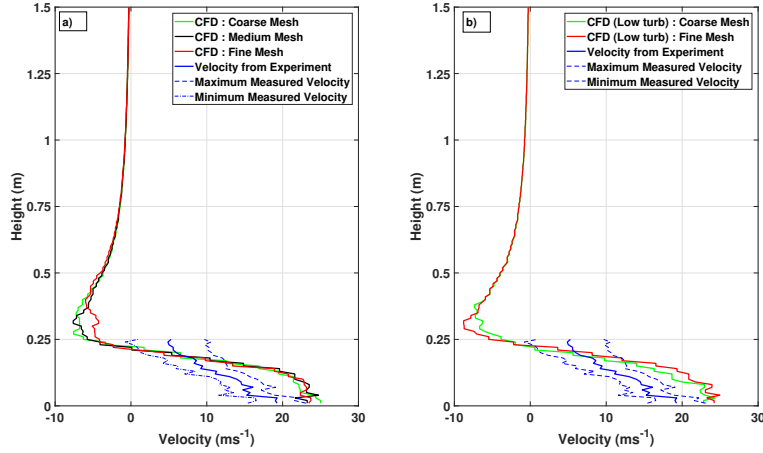

Figure 38: The mesh dependency on the maximum velocity with height at a location of $\frac{X}{D} = 1.5$. (a) Individual run turbulence level; (b) Ensemble average turbulence level.

Following this the pressure around the model buildings were compared for the meshes. Figures 40 and 41 illustrate that there is a slight difference for the varying mesh densities. The standard mesh has a brief suction prior to the primary vortex passing and the coarse mesh has a greater maximum pressure in
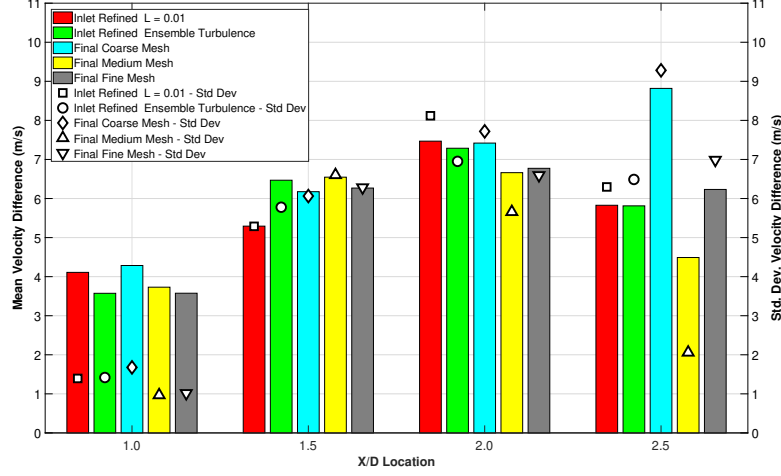
49

Figure 39: The mesh dependency of the dynamic Smagorinsky model on the revised mesh. Variation of maximum velocity with height.

the primary pressure peak region than the other two meshes. After the primary pressure peak the agreement is similar between the turbulence models.

However, considering the tap is only $30\,mm(\frac{Z}{D} = 0.03)$ from the floor, within the region which has been shown to overestimate the peak velocities the actual fit to the laboratory data is very good, especially for the standard and fine meshes. The good fit is also continued for the other taps, as illustrated by Figure 42.

It also became apparent from this entire investigation that it was the individual run turbulence which was more closely matching the laboratory results. The ensemble average turbulence at inlet gave a sharper pressure peak around the building with a greater maximum pressure, a sharper velocity peak in the velocity time histories with a greater maximum velocity and was also more sensitive to changes in the mesh density than the individual run case.
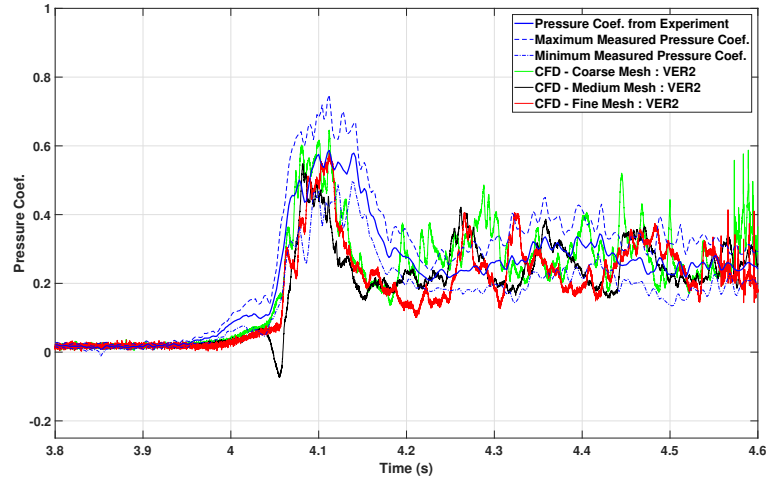
Figure 40: The mesh dependency of the pressure coefficient time history fit for the front face tap of the $60\,mm$ cube, individual run turbulence.
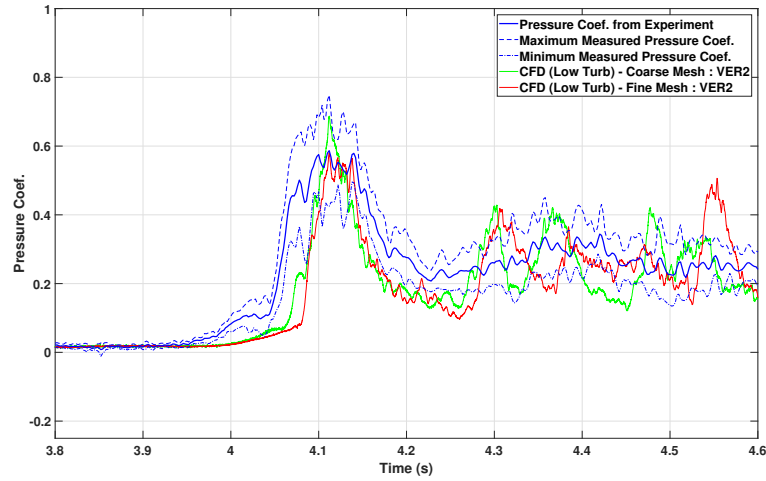

Figure 41: The mesh dependency of the pressure coefficient time history fit for the front face tap of the $60\,mm$ cube, ensemble turbulence.
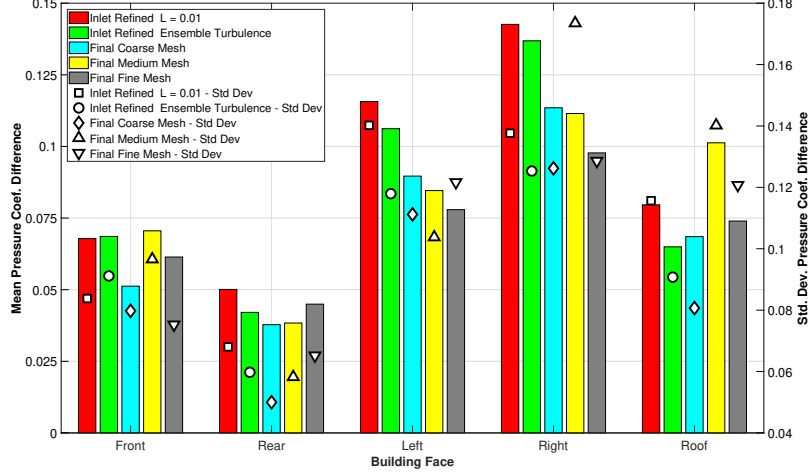
Figure 42: The mesh dependency of the dynamic Smagorinsky model on the revised mesh. Variation of pressure coefficient on surfaces of the $60\,mm$ cube building.

4. Conclusion

This paper sought to find most suitable turbulence model for modelling impinging jet outflow. To achieve this four different turbulence models were trialled and compared to the laboratory data collected by Jesson et al. (2015).

It was shown that the dynamic Smagorinsky LES turbulence model was most suitable. It was able to capture the velocity and pressure fluctuations at the inlet accurately, the velocity at pressure time histories at differing distances and heights from the centre of impingement and the pressures around a $60\,mm$ cube building.

There were some issues with the velocity time histories further from the centre of impingement, with the velocities in the CFD exceeding the laboratory data. This was found to be caused by the vortex translation velocity, which was far greater in the CFD than the laboratory simulations.

These issues were resolved by refining the mesh further, although the velocity height profile in the near wall region remained high when compared to the laboratory data. This difference was hypothesised to be caused by the lack

of surface roughness in the CFD simulation or an issue with the near wall turbulence model which was used.

The pressure match around the $60\,mm$ cube was not as good as the match found by Sengupta and Sarkar (2008) between their simulator and CFD simulation. This is likely to be because of some physical differences between the laboratory simulator of Jesson et al. (2015) and the CFD simulations. The simulator of Jesson et al. (2015) was far more complex, with a flaps mechanism which could not be modelled exactly without a large (and prohibitive) increase in CPU runtime. The match, given these differences, is reasonable.

Future work will include using the CFD model to examine the flow field around other model building types Jesson et al. (2015) examined, which includes differing building heights and shapes.

5. Acknowledgements

References

References

Balogh, M., A. Parente, and C. Benocci, 2012: Rans simulation of abl flow over complex terrains applying an enhanced $k - \varepsilon$ model and wall function formulation: Implementation and comparison for fluent and openfoam. *Journal of Wind Engineering and Industrial Aerodynamics*, **104-106**, 360–368.

Bazdidi-Tehrani, F., M. Kiamansouri, and M. Jadidi, 2016: Inflow turbulence generation techniques for large eddy simulation of flow and dispersion around a model building in a turbulent atmospheric boundary layer. *Journal of Building Performance Simulation*, **9(6)**, 680–698.

Billson, M., L. Eriksson, and L. Davidson, 2003: Jet noise prediction using stochastic turbulence modelling. *9th AIAA / CEAS Aeroacoustics Conference and Exhibit*, AIAA / CEAS.

Blocken, B., T. Stathopoulos, and J. Carmeliet, 2007: Cfd simulation of the atmospheric boundary layer: Wall function problems. *Atmospheric Environment*, **41**, 238–252.

Chay, M. and C. Letchford, 2002: Pressure distributions on a cube in a simulated thunderstorm downburst - Part A: stationary downburst observations. *Journal of Wind Engineering and Industrial Aerodynamics*, **90**, 711–732.

Craft, T., L. Graham, and B. Launder, 1993: Impinging jet studies for turbulence model assessment-II. An examination of the performance of four turbulence models. *International Journal of Heat and Mass Transfer*, **36(10)**, 2685–2697.

di Mare, L., M. Klein, W. P. Jones, and J.Janicka, 2006: Synthetic turbulence inflow conditions for large-eddy simulation. *Physics of Fluids*, **18(2)**, 025 107–1 − 025 107–11.

Egorov, Y. and F. Menter, 2007: Development and application of SST-SAS turbulence model in the DESIDER project. *2007 Symposium of Hybrid RANS-LES Methods*, Corfu, Greece, European Commision Research Directorate General, 261–270.

Fujita, T., 1985: Downburst: Microburst and macroburst. *University of Chicago Press, IL*, pp. 122.

Germano, M., U. Piomelli, P. Moin, and W. Cabot, 1991: A dynamic subgrid-scale eddy viscosity model. *Physics of Fluids A.*, **3(7)**, 1760–1765.

Gritskevich, M., A. Garburuk, J. Schütze, and F. Menter, 2012: Development of DDES and IDDES formulations for the k-ω shear stress transport model. *Flow, Turbulence and Combustion*, **88**, 431–449.

Haines, M., 2014: The simulation of non-synoptic effects and their implications for engineering structures. Ph.D. thesis, University of Birmingham.

Haines, M. and I. Taylor, 2018: Numerical investigation of the flow field around low rise buildings due to a downburst event using large eddy simulation. *Journal of Wind Engineering and Industrial Aerodynamics*, **172**, 12–30.

Haines, M., I. Taylor, M. Jesson, and M. Sterling, 2015: The numerical simulation of a pulsed impinging jet using modern turbulence models. *Proceedings of the 14th International Conference on Wind Engineering*, Porto Alegre, Brazil, June 2015, ICWE, ID 1869.

Holmes, J., 1992: Physical modelling of thunderstorm downdrafts by wind tunnel jet. *Second AWES Workshop*, Monash University, USA, AWES, 29–32.

Jesson, M., M. Sterling, C. Letchford, and M. Haines, 2015: Aerodynamic forces on generic buildings subject to transient, downburst-type winds. *Journal of Wind Engineering and Industrial Aerodynamics*, **137**, 58–68.

Kareem, A., 2012: Modelling of transient winds and their load effects on structures. *Proceedings of the 10th UK Conference on Wind Engineering*, University of Southampton, UK, September 2012, WES, 3–17.

Kim, Y., I. Castro, and Z.-T. Xie, 2013: Divergence free turbulence inflow conditions for large eddy simulations with incompressible flow solvers. *Computers and Fluids*, **84**, 56–68.

Knupp, K., 1985: Precipitating convective cloud downdraft structure: a synthesis of observations and modelling. Ph.D. thesis, Colorado State University, [Thesis available from: Atmospheric Science Paper No. 387 Dept. of Atmospheric Sciences, Colorado State University, Fort Collins, CO 80523].

Kornev, N. and E. Hassel, 2007: Method of random spots for generation of synthetic inhomogeneous turbulent fields with prescribed autocorrelation functions. *Communications in Numerical Methods in Engineering*, **23**, 35–43.

Lamberti, G., C. García-Sánchez, J. Sousa, and C. Gorlé, 2018: Optimizing turbulent inflow conditions for large-eddy simulations of the atmospheric boundary layer. *Journal of Wind Engineering and Industrial Aerodynamics*, **177**, 32–44.

LEMOS, 2015: LEMOS extensions for OpenFOAM 2.3.x, developed by Nikolai Kornev. Universität Rostock, URL `http://www.lemos.uni-rostock.de/en/downloads/cfd-software/`, [Online; accessed 15th August 2015].

Lilly, D., 1992: A proposed modification of the germano subgridscale closure method. *Physics of Fluids A.*, **4**, 633–635.

Lilly, D., R. A. Anthes, E.-Y. Hsie, and Y.-H. Kuo, 1967: The representation of small-scale turbulence in numerical simulation experiments. NCAR Manuscript NCAR Manuscript no. 281, National Center for Atmospheric Research, 24 pp.

Lin, W. and E. Savory, 2006: Large-scale quasi steady modelling of a downburst outflow using a slot jet. *Wind and Structures*, **9**, 419–440.

Mason, M., C. Letchford, and D. James, 2005: Pulsed wall jet simulation of a stationary thunderstorm downburst, Part A: Physical structure and flow field characterisation. *Journal of Wind Engineering and Industrial Aerodynamics*, **93**, 557–580.

Mason, M., G. Wood, and D. Fletcher, 2007: Impinging jet simulation of stationary downburst flow over topography. *Wind and Structures*, **10**, 437–462.

Mason, M., G. Wood, and D. Fletcher, 2009: Numerical simulation of downburst winds. *Journal of Wind Engineering and Industrial Aerodynamics*, **97**, 523–539.

McConville, A., M. Sterling, and C. Baker, 2009: The physical simulation of thunderstorm downbursts using an impinging jet. *Wind and Structures*, **12(2)**, 133–149.

Menter, F. and Y. Egorov, 2010: The scale-adaptive simulation method for unsteady turbulent flow predictions. Part 1: Theory and model description. *Flow, Turbulence and Combustion*, **85**, 113–138.

OpenFOAM, 2014: The OpenFOAM foundation website. OpenCFD Ltd., URL `http://www.openfoam.org/index.php`, [Online; last viewed 21st October 2014].

Palmén, E., 1951: *Compendium of meteorology*. American Meteorological Society, Boston, 599-620 pp.

Parente, A., C. Gorlé, J. van Beecl, and C. Benocci, 2011: A comprehensive modelling approach for the neutral atmospheric boundary layer: Consistent inflow conditions, wall function and turbulence model. *Boundary-Layer Meteorology*, **140**, 411–428.

Patruno, L. and M. Ricci, 2017: On the generation of synthetic divergence-free homogeneous anisotropic turbulence. *Computer Methods in Applied Mechanics and Engineering*, **315**, 396–417.

Poletto, R., T. Craft, and A. Revell, 2013: A new divergence free synthetic eddy method for the reproduction of inlet flow conditions for LES. *Flow, Turbulence and Combustion*, **91**, 519–539.

Roberts, R. and J. Wilson, 1984: Precipitation and kinematic structure of microburst producing storms. *22nd Conference on Radar Meteorology 10th-13th September 1984*, Zurich, 22nd Conference on Radar Meteorology, 71–76.

Selvam, R. and J. Holmes, 1992: Numerical simulation of thunderstorm downdrafts. *Journal of Wind Engineering and Industrial Aerodynamics*, **44(4)**, 2817–2825.

Sengupta, A. and P. Sarkar, 2008: Experimental measurement and numerical simulation of an impinging jet with application to thunderstorm microburst winds. *Journal of Wind Engineering and Industrial Aerodynamics*, **96(3)**, 345–365.

Shur, M., P. Spalart, M. Strelets, and A. Travin, 2008: A hybrid RANS-LES approach with delayed DES and wall modelled LES capabilities. *International Journal of Heat and Flow*, **29**, 1638–1649.

Spalart, P., 2001: Young-person's guide to detached-eddy simulation grids. NASA Technical Report NASA/CR-2001-211032, NASA, 23 pp., Langley research centre, Hampton, Virginia, 23681-2199.

Spalart, P., S. Deck, M. Shur, K. Squires, M. Strelets, and A. Travin, 2006: A new version of detached eddy simulation resistant to ambiguous grid densities. *Theoretical Computational Fluid Dynamics*, **20**, 181–195.

Spalart, P., W.-H. Jou, M. Strelets, and S. Allmaras, 1997: Comments on the feasibility of LES for wings and on a hybrid RANS/LES approach. *Advances in DNS/LES*, C. Liu and Z. Liu, Eds., Greyden Press, Columbus, OH, 137–147.

Sterling, M., C. Baker, P. Richards, R. Hoxey, and A. Quinn, 2006: An investigation of the wind statistics and extreme gust events at a rural site. *Wind and Structures*, **9(3)**, 193–216.

Vermeire, B., L. Orf, and E. Savory, 2011: Improved modelling of downburst outflows for wind engineering applications using a cooling source approach. *Journal of Wind Engineering and Industrial Aerodynamics*, **99**, 801–814.

von Karman, T. and L. Howarth, 1938: On the statistical theory of isotropic turbulence. *Proceedings of the Royal Society of London. Series A, Mathematical and Physical Sciences*, **164(917)**, 192–215.

Wang, L., M. McCullough, and A. Kareem, 2013: Modelling and simulation of non-stationary processes using wavelet and Hilbert transforms. *Journal of Engineering Mechanics*, **140(2)**, 345–360.

Yan, B. and Q. Li, 2015: Inflow turbulence generation methods with large eddy simulation for wind effects on tall buildings. *Computers and Fluids*, **116**, 158–175.

Yu, R. and X.-S. Bai, 2014: A fully divergence-free method for generation of inhomogeneous and anisotropic turbulence with large spatial variation. *Journal of Computational Physics*, **256**, 234–253.

Zheng, D.-Q., A.-S. Zhang, and M. Gu, 2012: Improvement of inflow boundary condition in large eddy simulation of flow around tall building. *Engineering Applications of Computational Fluid Mechanics*, **6(4)**, 633–647.